Research Article

Ende Wang*, Chenming Zhao, Qingquan Liu, and Mingming Du

Bayesian inference-based physics-informed neural network for performance study of hybrid nanofluids

https://doi.org/10.1515/ntrev-2025-0192
received November 21, 2024; accepted June 14, 2025

Abstract: Accurate prediction of thermophysical properties of hybrid nanofluids (HNFs) is a major challenge in thermodynamic applications. This research provides a computational framework to solve the complexity of heat transfer and flow physics in Al_2O_3–Cu/water HNFs. A reconstruction of the statistical microstructure of the fluid is constructed by the Karhunen–Loève expansion. The physical processes are modeled with a system of partial differential equations that model the interactions between the base fluid and dispersed nanoparticles. In the context of flow variables and entropy generation with sharp gradients, a Bayesian inference extension of the physics-informed neural network (PINN) is developed to improve prediction accuracy. Bayesian inference PINN (BIPINN) is the extension that infers posterior distributions of hidden thermal flow states, conditioned on prior physical laws. The framework is validated through many physical problems such as convective flow, thermal conduction, and fluctuation control. BIPINN shows improved accuracy over the finite element method while also showing improved generalization under sparse data while illustrating robustness of the framework while modeling complex thermal-fluid systems.

Keywords: Al_2O_3–Cu/water hybrid nanofluids, Karhunen–Loève expansion, Bayesian physics-informed neural network, thermal-fluid systems

*** Corresponding author: Ende Wang,** Faculty of Equipment Engineering, Shenyang Ligong University, Shenyang, 110159, Liaoning, China, e-mail: ende_wang@163.com
Chenming Zhao, **Qingquan Liu:** Faculty of Equipment Engineering, Shenyang Ligong University, Shenyang, 110159, Liaoning, China
Mingming Du: Faculty of Big Data, Yunnan Agricultural University, Kunming, 650000, Yunnan, China
ORCID: Ende Wang 0000-0001-6196-969X; Chenming Zhao 0009-0008-5919-9006; Qingquan Liu 0000-0003-4952-8079; Mingming Du 0009-0008-4484-8624

Nomenclature

$\mathcal{B}$	boundary condition operator in the heat conduction process of hybrid nanofluids
b	bias vector
C	covariance kernel
c	heat flow
c_p	specific heat capacity of hybrid nanofluids (J kg^{-1} K^{-1})
f	source term
H	heat flux (W/m^2)
L	linear differential operator in the heat conduction process of hybrid nanofluids
N	sensors
q	heat flow density of hybrid nanofluids (W m^{-2})
S	state of hybrid nanofluids
u	nanoparticle concentration (wt%)
W	weight matrix
x	independent variable

Greek symbols

τ	the correlation time
$\partial\Omega$	boundary dataset
Ω	measurement dataset
ϵ	independent Gaussian noise
θ	parameter set
v	velocity component
ρ	density of hybrid nanofluids (kg m^{-3})
κ	thermal conductivity of hybrid nanofluids (W m^{-1} K^{-1})

Subscripts

r	the scale of the covariance
hnf	hybrid nanofluids

ω temperature fluctuation domain of hybrid nanofluids
l layers of the network

1 Introduction

Nanotechnology has completely transformed modern heat transfer techniques. Nanofluids (NFs), in particular, are engineered fluids that contain suspended nanoparticles [1]. These particles are usually metallic or non-metallic, and the incorporation of them into a base fluid enhances its features of thermophysics, such as conductive heat, viscosity, and specific heat. When nanoparticles are added to water or ethylene glycol, NFs result, which possess higher heat transfer characteristics than traditional fluids [2]. In order to improve the thermal and physical properties of NFs, the choice of the nanoparticles is very important [3]. It was shown that some nanoparticles such as alumina have great mobility and stability, but they still have low thermal conductivity. Moreover, certain nanoparticles like zinc, copper, silver, and aluminum have high conductivity but have low stability and reactivity. Hence, to remedy these problems, research works showed that it is possible to make a mixture of nanoparticles in a base fluid and obtain a new class of NF called hybrid nanofluids (HNFs) [4].

HNFs, combining different nanoparticles, outperform single-phase NFs in heat transfer efficiency and other properties [5]. Due to the interesting behavior of HNFs in rising characteristics of heat conductivity attracts many researchers to consider HNFs in their studies to deal with real problems of the word. Beyond industrial applications, HNFs are also being applied in biomedical fields [6]. Shah *et al.* [7] studied the incorporation of three distinct nanoparticles in blood within the context of cubic autocatalysis holds, which have significant potential for enhancing biomedical applications, particularly in targeted drug delivery and therapeutic interventions. The adaptability of NFs across different sectors proves that they can be a transformative technology for industrial and medical applications, with great potential for improvement in performance and efficiency compared to the conventional fluids.

HNFs show great promise for thermal management but face challenges such as nanoparticle stability, fluid compatibility, and precise tuning of thermophysical properties. Suresh *et al.* [8] studied the stability of the NFs was ensured by pH and Zeta potential measurements. Advances in nanotechnology are overcoming these barriers, making HNFs essential for future applications. Hemmat Esfe *et al.* [9] studied the rheological characteristics of HNFs, which are tailored to different applications.

Al_2O_3-Cu/water is one of the attractive choices for improving heat transfer in industries like electronics cooling, power generation, and chemical processing [10], as copper is one the most thermally conductive metal that enhances the thermal conductivity significantly and Al_2O_3 adds stability and strength. Khalil *et al.* [11] investigated the flow characteristics and heat transfer behavior of a copper-alumina HNFs suspended in water over a porous exponentially stretching surface. Khashiie *et al.* [12] investigated the impact of various radiation parameters, electromagnetohydrodynamics, and form factors of the nanoparticles on the Al_2O_3-Cu/water HNFs over a Riga plate subjected to stretching and shrinking effects. Tiam Kapen *et al.* [13] investigated a stability analysis of Al_2O_3-Cu/water HNFs flow between two parallel and stationary plates filled with a porous medium. Furthermore, Ayub *et al.* [14] investigates taking water as base fluid and the three nanoparticles are copper oxide (CuO), aluminum oxide (Al_2O_3), and titanium dioxide (TiO_2). Heat transport analysis is made through quadratic convection, magnetic field, and thermal radiation. Ayub *et al.* [15] investigated the influences of orthogonal/inclined magnetic field, thermal radiation, Brownian motion, thermophoresis, activation energy, and external source variation on magnetized radiative Cross NF.

To tackle these difficulties, Yoon *et al.* [16] started exploring artificial intelligence techniques, including deep learning (DL) and regression, to handle large datasets and improve prediction accuracy. Leveraging experimental data, data-driven modeling has become an increasingly prominent approach [17]. DL algorithms, which rely on data-driven techniques, are gaining substantial attention in scientific and engineering disciplines [18]. This rise is supported by advances in computational power, lower sensor costs, and increased storage capacities, enabling broader data access and faster algorithm development. Unlike traditional methods that need a detailed understanding of system mechanics, data-driven approaches offer viable solutions to complex problems in HNFs dynamics and heat transfer that are challenging to address with deterministic models [19]. Kanti *et al.* [20] utilized the Boosted Regression Tree machine learning model to predict the thermophysical properties of HNF based on the temperature (T) and mixing ratio (R) of NFs. Marulasiddeshi *et al.* [21] employed experimental data to establish a cascaded feed-forward neural network model for modeling and predicting the thermal conductivity and viscosity of NFs. Kanti *et al.* [22] further explored the Bayesian-optimized neural network (ANN) model, in combination with K-fold cross-validation, to model and predict viscosity (VST), specific heat capacity (SHC), and thermal conductivity (TC).

Partial differential equations (PDEs) assume a vital role in the domains of natural science and engineering.

From the Navier-Stokes equations in fluid mechanics to the heat equation in heat conduction, PDEs are utilized to depict various complex physical phenomena and system behaviors. Nevertheless, solving PDEs has consistently been a significant challenge in scientific computing. Traditional numerical methods, such as finite element analysis [23] and finite difference techniques [24], often require substantial computational resources and may struggle with complex geometries or highly nonlinear problems. Although they are capable of offering effective approximate solutions in numerous circumstances, they typically demand a considerable amount of computing resources, particularly when handling high-dimensional issues, complex geometries, or nonlinear equations.

A notable example is the work by Akbar *et al.* [25], where the PDEs were transformed into dimensionless nonlinear ordinary differential equations *via* similarity transformation and solved using a neural network trained by the Levenberg-Marquardt algorithm. This study examined the two-dimensional steady-state incompressible boundary layer flow of the HNFs (Al_2O_3-Cu/water) over a porous stretching sheet. The model analyzed the influences of factors such as the thermal Biot number, NF concentration, and porosity of the porous medium on the fluid temperature, velocity, and thermal distribution. Alghamdi *et al.* [26] examined the flow properties of the Eyring-Powell fluid with double-layer composite convective heating around an elevated stretched cylinder. By means of numerical solution techniques (BVP4C, three-stage Lobatto IIIa formula) and parameter sensitivity analysis, the effects of key parameters (curvature parameter, fluid parameters, mixed convection parameter, buoyancy ratio, thermal stratification parameter, solute stratification parameter, and inclination angle) on fluid velocity, heat transfer, and mass transfer characteristics were investigated. Shah *et al.* [27] employed the backpropagation technique of neural networks to study the influence of Maxwell fluid on the flow of ternary hybrid nanoparticles through a Riga plate under convective boundary conditions. The model analyzed the impacts of parameters such as Maxwell fluid parameters, Biot number, thermal radiation, *etc.*, on flow and heat transfer. The aforementioned studies simplify the solution process by transforming PDEs into ordinary differential equations or other reduced-order formulations. However, such approaches often necessitate problem-specific assumptions or approximations, which may compromise the fidelity of the solution by omitting essential physical information or nonlinear interactions inherent to the original governing equations.

To address these challenges, Xu *et al.* [28] introduced a data-driven approach for solving PDEs, which embeds fundamental physical laws within the PDE framework. This method has gained traction for its ability to make reasonably accurate predictions of unknowns, even with limited data. In this area, two key techniques are Gaussian process regression (GPR) for PDEs, introduced by Bertrand *et al.* [29], and physics-informed neural networks (PINNs), developed by Lu *et al.* [30]. GPR is widely used because it incorporates uncertainty quantification, but as Mishra and Molinaro [31] noted, traditional GPR struggles with nonlinear PDEs. In contrast, Yu *et al.* [32] examined the effectiveness of PINNs in addressing both forward and inverse problems. Research by Lorenzen *et al.* [33] demonstrated successful applications of PINNs across various fields to solve PDE-related physical problems. Shi *et al.* [34] found that PINNs are particularly effective in modeling nonlinear PDE systems based on physical laws, such as those required to simulate complex thermodynamic processes like entropy generation and thermal rheology.

Entropy generation, a concept fundamental to thermodynamic systems, results from irreversible processes and is known as "entropy production." Khan *et al.* [35] noted that NFs often experience irreversible events during flow and heat exchange, including dispersion, fluid friction from viscosity, heat transfer, and permeation. These processes contribute to the total entropy of the medium. Entropy generation reflects the irreversibility inherent in thermal processes, driven by factors such as heat flow along thermal gradients, laminar heat transfer characteristics, and viscous fluid interactions. From an engineering standpoint, understanding and controlling the irreversible factors that contribute to entropy generation is highly valuable. Entropy reflects system disorder and is directly linked to thermodynamic performance. Therefore, reducing entropy generation is crucial for improving the efficiency of thermodynamic systems. For example, Oyelakin and Sibanda [36] investigated entropy generation in Casson nanofluid flow over moving wedges, offering insights into radiation and fluid transport variability. Shutaywi and Shah [37] studied the impact of various parameters on the virtual flow characteristics of HNFs, using entropy optimization as an evaluative tool. Rashed *et al.* [38] investigated the flow of ternary HNFs containing gyrotactic microorganisms in microchannels, analyzing the effects of magnetic fields, thermophoresis, and Brownian motion. Additionally, Lone *et al.* [39] analyzed entropy generation in HNFs under nonlinear convection effects.

In thermal media, entropy optimization involves estimating unknown heat flux or thermophysical properties of nanomaterials through temperature measurements. This estimation process can be approached *via* parameter estimation or function estimation methods. A direct way to determine the solution using a deterministic approach is the least squares method by finding the mismatch between observed data and the forward model [40]. Various deterministic techniques,

such as generalized or weighted least squares, conjugate-gradient method [41], and iterative regularization methods have been developed for parameter and function estimations in heat conduction problems. These deterministic methods are easy to implement and predict single values of model parameters through optimization to minimize the difference between measurement data and model prediction. However, these methods do not provide higher-order statistics of the parameter estimates. Khatoon *et al.* [42] addressed this challenge by simplifying it to parameter estimation, assuming known functional forms of boundary conditions. However, when prior information on boundary functions is unavailable, the problem expands to function estimation within an infinite-dimensional function space.

To model the uncertain heat flux distribution in NFs, Pulch [43] utilized the Karhunen-Loève (K–L) expansion method. This method decomposes the physical field into a linear combination of orthogonal basis functions, each weighted by random variables, represented as coefficients or modes in an infinite series. Chandra *et al.* [44] employed the K–L expansion to derive continuous heat flux distributions from limited measurement data, incorporating essential regularization to stabilize the process. Through K–L expansion, the complex problem of estimating time-varying heat flux at discrete points reduces to determining a few principal coefficients. Jiang *et al.* [45] applied K–L dimensional reduction to extract core features from high-dimensional heat flux data, effectively simplifying the data while retaining key physical information. Rui *et al.* [46] further advanced this by feeding the reduced data into a PINN, leveraging PINN's ability to integrate physical laws for learning and predicting the heat flux field. Kiyani *et al.* [47] demonstrated that, with training, PINN captures intricate dynamic behaviors in the heat flux field, accurately representing fluid dynamics and heat transfer processes to yield precise heat flux predictions. However, Soibam *et al.* [48] noted that PINN lacks inherent uncertainty quantification, which can limit its use, particularly in noisy data environments. In previous work, Yeongmin *et al.* [49] incorporated physical laws into a loss function and paired it with a generative adversarial network to quantify and propagate system uncertainty, using latent variable models as probabilistic representations. Son *et al.* [50] emphasized that accurate PINN optimization requires high-order automatic differentiation and multi-objective nonlinear optimization, minimizing the loss function to near zero while integrating differential equations, initial conditions, and boundary conditions. Jang *et al.* [51] observed that this complexity may hinder convergence and reduce training efficiency.

Hence, Chandra Yoo [52] proposed a hybrid PINN + Interior-point algorithm (IPA) framework to investigate bioconvective NF flow over an inclined stretching surface. The IPA synergistically integrates line search and trust-region methodologies to rapidly identify optimal solutions during the optimization process, by conducting searches within the interior of the feasible domain rather than along constraint boundaries. Jawad *et al.* [53] proposed a hybrid PINN + homotopy analysis method (HAM) framework to investigate time-dependent Jeffrey HNFs flow in rotating porous media with coupled thermosolutal convection. By constructing a homotopic mapping operator, this methodology decomposes the original strongly nonlinear problem into a sequence of linear subproblems through continuous deformation of the solution space, enabling systematic approximation of the governing system's dynamical behavior. Notably, the analytic solutions derived from HAM serve as high-fidelity initial conditions for PINNs training, significantly accelerating convergence by circumventing local minima traps associated with naive random initialization. Bhaumik *et al.* [54] presented that the PINN + Bayesian optimization was employed to analyze the propagation of weakly nonlinear waves in viscoelastic arterial conduits filled with viscous NFs. Regarding the perturbed Burgers equation and the perturbed KdVB equation, the model post Bayesian optimization reached a lower loss value within a reduced number of iterations.

Building on this, Yang *et al.* [55] introduced Bayesian PINN (B-PINN) to solve linear and nonlinear PDEs with noisy data. The trained model leverages Bayes' theorem to update hypothesis probabilities based on sensor or environmental data, a method used in NF research to infer physical mechanisms through application-driven evolution [56]. Bararnia and Esmaeilpour [57] extended PINN applications to address viscosity and thermal boundary layer issues in unseen data.

In summary, hybrid NFs flow and heat transfer exhibit complex, nonlinear dynamics, due to the inherent randomness and microstructural complexity of HNFs, leading to high data acquisition costs and varying data quality. Consequently, this study establishes an integrated computational framework to analyze the momentum and heat transfer characteristics of Al_2O_3-Cu/water HNFs. Employing the K–L expansion reduces model dimensionality, high-dimensional data are compressed using the K–L expansion to isolate essential features and significantly reduce computational burden. This reduced representation serves as input to Bayesian inference PINN (BIPINN), which leverages the physical structure encoded in PDEs to refine predictions and assess uncertainty *via* Bayesian inference. The incorporation of PDE-derived constraints further restricts the solution space to physically plausible outcomes, thereby enhancing both the accuracy and reliability of the model. By leveraging a BIPINN that integrates data with physical laws, this approach effectively addresses unsolvable or

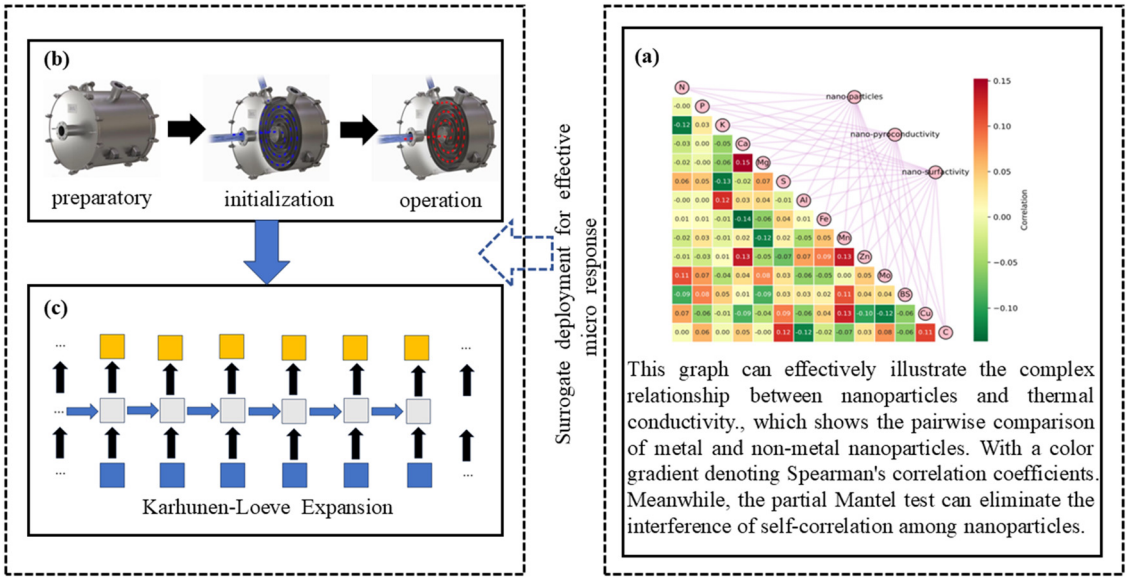

Figure 1: Nanoparticle selection and fluid heat flux modeling. (a) Heat transfer correlation of nanoparticles. (b) Database generation *via* SHE. (c) Surrogate development.

challenging problems under uncertain parameter conditions, minimizing dependence on data quality and volume. This study enhances understanding of heat transfer and flow mechanisms in HNFs, offering valuable insights for developing efficient thermal management systems.

2 Problem formulation

The heat flux for the Al_2O_3-Cu/water HNFs used for flow heat transfer in a spiral heat exchanger (SHE) was studied in discrete time, $H(t)$, and is taken as heat flux values at discrete time steps. However, modeling heat fluxes requires a large number of discrete points to recover the continuous function from finite data, so we introduce the K–L extended agent model as shown in Figure 1.

Convert the surrogate model into a reduced-dimensional inference of truncated weight sequences of K–L modes, $H(t)$ is parametrized using K–L expansion as

$$H(t) = \langle H(t) \rangle + \sum_{k=1}^{\infty} \sqrt{\lambda}_k \phi_k(t) c_k, \tag{1}$$

where λ_k and ϕ_k are the ordered eigenvalues and corresponding eigenfunctions of the covariance kernel and $c_k \sim \mathcal{N}(0, 1)$. The covariance kernel is chosen from the exponential conjugate family given as

$$C_r(t_1, t_2) = r \exp\left(-\frac{|t_1 - t_2|^2}{2\tau^2}\right). \tag{2}$$

The correlation time τ is considered known and the scale r of the covariance is considered to be a hyperparameter provided with gamma, $r \sim \Gamma(\gamma, \beta)$.

$$f(r, \beta, \gamma) = \frac{\beta^{\gamma}}{\Gamma(\gamma)} r^{\gamma-1} \exp(-\beta r), \tag{3}$$

$$\Gamma(\gamma) = \int_0^{+\infty} r^{\alpha-1} e^{-r} \mathrm{d}r, \tag{4}$$

where γ is the shape parameter, which denotes the number of incidents; β is the scale parameter, which denotes frequency of single events. λ_k and ϕ_k are solved using the Fredholm equation [58].

$$\int_D C(t_1, t_2)\phi_k(t_2)\mathrm{d}t_2 = \lambda_k \phi_k(t_1). \tag{5}$$

The covariance kernel, which is symmetric and positive definite, allows us to apply Mercer's theorem. This theorem enables the decomposition of the kernel into a series of orthogonal eigenfunctions and corresponding eigenvalues, which are essential for the Karhunen–Loève expansion [59].

$$C(t_1, t_2) = \sum_{k=1}^{\infty} \lambda_k \phi_k(t_1)\phi_k(t_2). \tag{6}$$

Approximating the heat flux by a truncated n term K–L expansion

$$H_n(t) = \langle H(t) \rangle + \sum_{k=1}^{n} \sqrt{\lambda}_k \phi_k(t) c_k. \tag{7}$$

The covariance kernel of H_n is

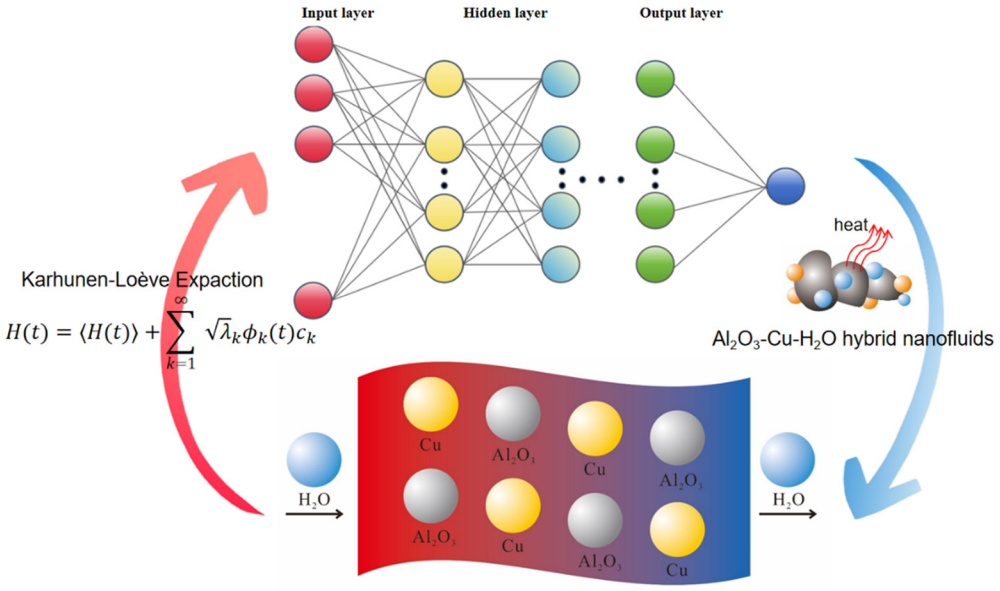

Figure 2: Neural network-driven heat transfer model for HNFs.

$$C(t_1, t_2) = \sum_{k=1}^{n} \lambda_k \phi_k(t_1)\phi_k(t_2), \tag{8}$$

which converges to equation (6) as $n \to \infty$, and using K–L expansion achieves the problem transformation.

3 Methodology

3.1 PINN method

The HNFs heat flux H is truncated by the K–L extension into heat flow c, which can be approximated using a neural network with L-layer, as shown in Figure 2.

The network is represented as follows:

$$c_\theta(x) = N(x; W, b) = f_L \bigodot f_{L-1} \bigodot \cdots \bigodot f_1(x), \tag{9}$$

where $\bigodot$ denotes Hadamard product. For the fully connected feedforward neural network, the function $f_i(x_i, \theta_i)$ consists of an affine transformation and nonlinear activation function and can be expressed as

$$f_i(x_i; W_i, b_i) = \alpha_i(W_i \cdot x_i + b_i). \tag{10}$$

Thus, the connection between adjacent layers is

$$c^l = \alpha_l(W_l^T c^{l-1} + b_l), \tag{11}$$

where $\mathbf{W}_l$ and $\mathbf{b}_l$ represent the weight matrix and bias vector of the layer, α_l is the activation function that provides nonlinear features to the neural network [60].

Accurately capturing the interplay between entropy changes and rheological properties allows for a deeper understanding of the thermodynamic and flow characteristics of fluids and providing accurate predictions for the thermal properties of NFs. In the process of heat conduction in HNFs, the boundary value problem (BVP) usually involves transforming the heat flow into complex PDEs, and can be expressed as

$$\begin{aligned} L_x(c;\lambda) &= f, x \in \Omega, \\ \mathcal{B}_x(c;\lambda) &= b, x \in \partial\Omega, \end{aligned} \tag{12}$$

where L_x is a linear differential operator, $\mathcal{B}_x$ is a boundary condition operator acting on the boundary, $\partial\Omega$, $c = c(x)$ is the solution of the PDE, λ is the vector of parameters in the PDE, and $f = f(x)$ is the source term.

In forward problems, λ is prescribed, and hence our goal is to infer the solution $c = c(x)$ at every $x \in \Omega$ and quantify its uncertainty.

In inverse problems, λ is also to be inferred from the data. We consider the scenario where available dataset Ω are scattered noisy measurements of N_c, N_b, and N_f from sensors: $\Omega = \Omega_c \cup \Omega_b \cup \Omega_f$, where $\Omega_c = \{(x_c^{(i)}), \bar{c}^{(i)}\}_{i-1}^{N_c}$, $\Omega_b = \{(x_b^{(i)}), \bar{b}^{(i)}\}_{i-1}^{N_b}$, $\Omega_f = \{(x_f^{(i)}), \bar{f}^{(i)}\}_{i-1}^{N_f}$, the measurements from $\{\Omega_c, \Omega_b, \Omega_f\}$ are represented as

$$\begin{aligned} \bar{c}^{(i)} &= c(x_c^{(i)}) + \epsilon_c^{(i)}, i = 1, 2 \ldots N_c, \\ \bar{b}^{(i)} &= b(x_b^{(i)}) + \epsilon_b^{(i)}, i = 1, 2 \ldots N_b, \\ \bar{f}^{(i)} &= f(x_b^{(i)}) + \epsilon_f^{(i)}, i = 1, 2 \ldots N_f, \end{aligned} \tag{13}$$

where $\epsilon_c^{(i)}$, $\epsilon_b^{(i)}$, $\epsilon_f^{(i)}$ are the independent Gaussian noise with zero mean. Note that the size of the noise could be different

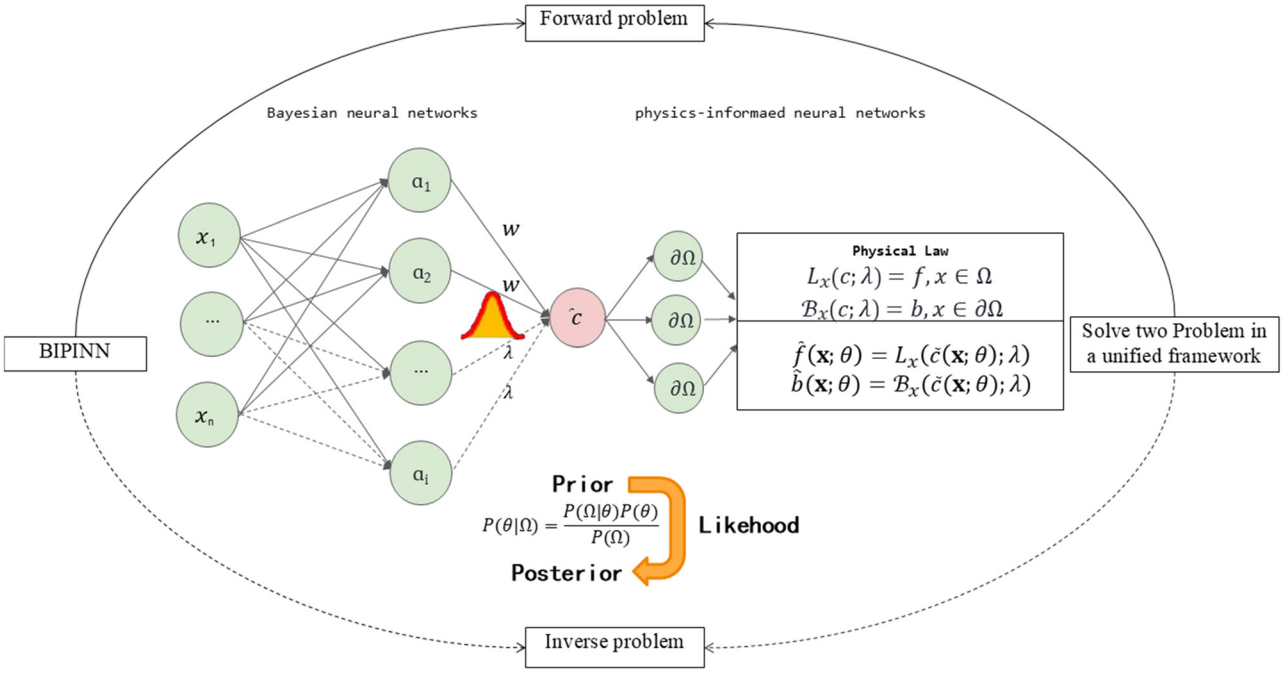

Figure 3: Physical information system based on Bayesian inference.

among measurements of different terms, and even between measurements of the same terms in the PDE. It can be seen that the complexity of the interaction between the base fluid and the nanoparticles makes the experimental and numerical simulation methods on HNFs limited by high economic and computational costs.

3.2 BIPINN method

In view of the above study, we propose BIPINN to predict the heat transfer characteristics of HNFs, Figure 3.

BIPINN starts from representing heat fluid c with a surrogate model $\tilde{c}(\mathbf{x};\theta)$. Since the forward problems and inverse problems are formulated in the same framework, we use θ to represent the vector of all the unknown parameters in the surrogate models for the solutions and parameters. Equation (12) is transformed into

$$\tilde{f}(\mathbf{x};\theta) = L_x(\tilde{c}(\mathbf{x};\theta);\lambda), \tilde{b}(\mathbf{x};\theta) = \mathcal{B}_x(\tilde{c}(\mathbf{x};\theta);\lambda). \quad (14)$$

Then, the likelihood can be calculated as

$$P(\Omega \mid \theta) = P(\Omega_c|\theta)P(\Omega_f|\theta)P(\Omega_b|\theta),$$
$$P(\Omega_c \mid \theta) = \prod_{i=1}^{N_c} \frac{1}{\sqrt{2\pi\sigma_c^{(i)^2}}} \exp\left(-\frac{(\tilde{c}(x_c^{(i)};\theta) - \bar{c}^{(i)})^2}{2\sigma_c^{(i)2}}\right),$$
$$P(\Omega_f \mid \theta) = \prod_{i=1}^{N_f} \frac{1}{\sqrt{2\pi\sigma_f^{(i)^2}}} \exp\left(-\frac{(\tilde{f}(x_f^{(i)};\theta) - \bar{f}^{(i)})^2}{2\sigma_f^{(i)2}}\right), \quad (15)$$
$$P(\Omega_b \mid \theta) = \prod_{i=1}^{N_b} \frac{1}{\sqrt{2\pi\sigma_b^{(i)^2}}} \exp\left(-\frac{(\tilde{b}(x_b^{(i)};\theta) - \bar{b}^{(i)})^2}{2\sigma_b^{(i)2}}\right).$$

Finally, the posterior is obtained from Bayes' theorem.

$$P(\theta|\Omega) = \frac{P(\Omega|\theta)P(\theta)}{P(\Omega)} \approx P(\Omega|\theta)P(\theta). \quad (16)$$

Usually, the calculation of $P(\theta)$ is analytically intractable, hence the solution is approximated by random sampling. To give a posterior c at any x, we can sample from $P(\theta \mid \Omega)$, denoted as $\{\theta^{(i)}\}_{i=1}^{M}$, and then obtain statistics from samples $\{\tilde{c}(x;\theta^{(i)})\}_{i=1}^{M}$.

The mean value of $\{\tilde{c}(x;\theta^{(i)})\}_{i=1}^{M}$ represents the prediction of $c(x)$, the standard deviation quantifies the uncertainty.

This method not only improves the prediction accuracy of the heat transfer characteristics of HNFs, but also performs better in the case of scarce and noisy data.

In the current research, we remark that all the information of boundary conditions and source terms come from experimental measurements. In contrast to experimental data acquisition, which is costly and of variable quality, BIPINN is able to construct suitable datasets in the presence of unknown parameters or boundary conditions, which significantly reduces the dependence on data quality and quantity, and allows us to effectively infer unseen or hidden thermophysical properties in HNFs flows.

The key idea of BIPINN is to encode physical laws into loss function by adding a penalty term to constrain the space of admissible solutions.

Concretely, equation (12) is transformed into the problem of minimizing the loss function. Then, to measure the difference between the BIPINN and actual observations, physical laws, the loss function is defined as

$$\mathcal{L}(\theta) = w_f \mathcal{L}_f(\theta; \mathcal{T}_f) + w_b \mathcal{L}_b(\theta; \mathcal{T}_b) + w_c \mathcal{L}_c(\theta; \mathcal{T}_c), \quad (17)$$

where

$$\begin{aligned} \mathcal{L}_f(\theta; T_f) &= \frac{1}{|T_f|} \sum_{\mathbf{x} \in T_f} \|f(t, \mathbf{x})\|^2, \\ \mathcal{L}_{\boldsymbol{b}}(\theta; T_{\boldsymbol{b}}) &= \frac{1}{|T_b|} \sum_{\boldsymbol{x} \in T_b} \|\mathcal{B}(\mathbf{x}) - b\|^2, \\ \mathcal{L}_{\mathbf{c}}(\theta; T_{\mathbf{c}}) &= \frac{1}{|T_c|} \sum_{\mathbf{x} \in T_c} \|\hat{\mathbf{c}}(\mathbf{x}) - c(\mathbf{x})\|^2. \end{aligned} \quad (18)$$

w_f, w_b as well as w_c are the hyper-parameters of weights. f represents the PDE residual in equation (12). θ represents the weights and bias of the BIPINN. $\hat{c}$ denotes the output of the BIPINN. T_f, T_b, and T_c denote the training points from PDE residual, boundary, and data constraints, respectively.

The boundary functions and data constraints contain special solutions to the PDEs. This mathematical framework of a "general solution + particular solution" inherently satisfies the specific prerequisite conditions of the particular solution, thereby accelerating BIPINN convergence toward the optimal gradient direction.

4 Mechanistic framework of BIPINN

This section provides a detailed account of the working mechanism of BIPINN. We expound upon it in terms of data preparation, the training process of BIPINN, the establishment of the loss function, the functionality of the loss function, the optimization strategy for the loss function, the convergence criterion, and the verification scheme.

4.1 Data preparation

1. The initial condition points and boundary conditions used for training are obtained through random sampling.
2. Dynamically adjusting sampling parameters to optimize convergence is an important strategy in Bayesian inference. If the training data can cover the entire solution space of the problem and be uniformly distributed, the model is more prone to learning the global optimal solution, thereby enhancing the convergence.

It is mainly related to the configuration of the Markov Chain Monte Carlo (MCMC) sampler. Specifically, the code uses Pyro's MCMC and NUTS (No-U-Turn Sampler) to perform random sampling within the defined domain to fit the model. The following methods are used to dynamically adjust sampling parameters to improve convergence and sampling efficiency:

(1) Adaptive mass matrix can help the sampler better adapt to the geometric shape of the target distribution, thereby improving sampling efficiency.
(2) Dynamic adjustment of step size: During the sampling process, the step size is dynamically adjusted based on the acceptance rate of the sampler. Generally, an acceptance rate between 0.6 and 0.9 is considered ideal.

4.2 Training process of BIPINN

4.2.1 Choice of optimization algorithms

In engineering applications, NFs are frequently employed to enhance heat transfer efficiency. Nevertheless, the heat transfer and flow issues of HNFs involve multiple physical fields (such as velocity, temperature, and concentration), featuring complex gradient variations. The Adam optimizer integrates the merits of momentum and adaptive learning rate (Adagrad), and is capable of dynamically adjusting the learning rate based on the gradient of parameters. This proves highly effective in handling complex nonlinear PDEs. LBFGS is an optimization algorithm based on the quasi-Newton method, which adjusts parameters by approximating the Hessian matrix, enabling more efficient optimization of non-linear problems and further reduction

in the loss function. Consequently, in this work, the Adam –optimizer is utilized for the pre-training of the neural network and the Limited-memory Broyden–Fletcher–Goldfarb–Shanno (L-BFGS) optimization algorithm is further adopted for further optimization, with the aim of improving the accuracy of the model.

4.2.2 Adjustment of the learning rate

The initial learning rate is set to 1×10^{-3}, Adam dynamically adjusts the learning rate by calculating the first moment (mean value) and the second moment (uncentered variance) of the gradients, thereby automatically adapting to different parameter scales during the training process.

4.3 Loss function construction

Through BIPINN, researchers can directly embed these complex physical phenomena into the loss function of the neural network, thereby solving for the flow, temperature, and concentration fields that satisfy all physical constraints. The loss function consists of the following components:

1. PDE residual loss: This part of the loss ensures that the network's output satisfies the PDEs governing the flow of the HNFs. The PDE residuals are calculated using automatic differentiation techniques and reflect the deviation between the network's predictions and the physical laws.
2. Boundary condition loss: This part of the loss ensures that the network's output satisfies the given boundary conditions at the boundaries. Boundary conditions are one of the physical constraints of the problem, and for the HNFs flow problem, they may include the values of velocity, temperature, and concentration at the boundaries.
3. Initial condition loss: This part of the loss ensures that the network's output satisfies the given initial conditions at the initial time. Initial conditions are crucial for describing the initial state of the HNFs flow.

When the value of the loss function drops below a very small threshold (set to 10^{-5} in this work), the model is considered to have converged.

4.4 Functionality of the loss function

1. Increasing the quantity of hidden layers can enhance the nonlinear expression capacity of the model. However, an overly complex model might exhibit overfitting, and an excessively large batch size can also reduce the generalization performance. Consequently, this model, taking the loss function as the criterion, determined the optimal number of layers and nodes.
2. The goal of this study is to analyze the flow, heat transfer, and mass transfer characteristics of NFs under the condition of multi-physical field coupling. BIPINN is capable of effectively integrating physical laws and data-driven models. We directly incorporate these complex physical phenomena into the loss function of the neural network, thereby solving the flow, temperature, and concentration fields that satisfy all physical constraints.

4.5 Optimization strategies for loss function

Constructing the loss function in PINN represents a challenge for optimization techniques since it involves multi-objective optimization during the training process. This might result in gradient imbalance during backpropagation and consequently lead to inaccurate predictions. To solve this problem, the study utilizes an optimization algorithm combining Adam and L-BFGS to dynamically adjust the weights and biases of the network, such that the output of the network satisfies physical laws and boundary conditions as closely as possible.

4.6 Convergence criteria

1. During the training process, the loss function gradually decreases as training progresses. Training is stopped when the decrease in the loss function is less than a certain threshold, specifically
$$\frac{|\mathcal{L}_{\text{current}} - \mathcal{L}_{\text{previous}}|}{\mathcal{L}_{\text{previous}}} < 10^{-5}.$$
2. All the research cases in this study were trained with adequate numbers of training rounds and iterations. The optimizer has built-in parameters max_iter = 50,000 and max_eval = 50,000. max_iter represents the maximum number of iterations, and max_eval represents the maximum number of function evaluations (*i.e.*, the number of times the loss function is calculated). These two parameters together form the convergence criterion for the optimizer stage. When either limit is reached, the optimization process will stop.
3. The L-BFGS optimizer employs the strong Wolfe conditions for line search. The strong Wolfe conditions are a

strategy for controlling step size selection, ensuring that the step size in each iteration is neither too large nor too small, thereby guaranteeing the stability and convergence of the optimization process.

4.7 Methods for comparing the reference solution with the BIPINN predicted solution

In this section, the performance of the proposed computational framework presented herein on multiple PDEs is evaluated to validate its efficacy and compared with the baseline algorithm (the vanilla PINN method) and COSMOL finite element analysis. The conventional approaches serving as reference solutions in this study encompass the analytical solution of PINN and the numerical solution of COSMOL. To quantify the disparity between the predicted solution and the reference solution, the results are presented in the form of heat maps.

All the numerical implementations in this work are encoded using Pytorch and computed on an NVIDIA Tesla T4 GPU.

5 Simulation results and analysis

5.1 Two-dimensional unsteady convection-diffusion

In the nuclear industry, two-dimensional unsteady convection-diffusion equations describe the convection and diffusion processes of substances (such as radioactive materials, heat, or other important substances) in space. For the two-dimensional unsteady convection-diffusion problem in HNFs, the proposed computational framework, which integrates K–L expansion with B-PINN, enables accurate prediction and simulation of fluid behavior and heat conduction. Unlike traditional finite difference methods [61], this approach bypasses the need for explicit discretization. Instead, the physics-informed neural network learns the physical principles embedded in the PDEs, training the network to approximate the fluid flow solution. The two-dimensional unsteady convection-diffusion equation is defined as

$$\frac{\partial u}{\partial t} + c\frac{\partial u}{\partial x} = 0, \tag{19}$$

where $u(x, t)$ denotes the nanoparticle concentration, varying with time t and spatial coordinate x. c represents the convective velocity in the x direction. Periodic boundary conditions are imposed on the equation, specified at $x = 0$ and 1.

$$u(x_1, t) = u(x_2, t). \tag{20}$$

Namely, the concentration assumes the identical value at the two opposing boundaries. The reasons for selecting periodic boundary conditions are as follows:

1. In two-dimensional unsteady convective diffusion problems, periodic boundary conditions enable researchers to simulate the behavior of an infinitely large system with periodic characteristics within a smaller computational domain. This treatment not only reduces the computational cost but also enhances the universality of the model, allowing it to be applied to systems of different scales and geometries.
2. In the convective diffusion process, the movement of the fluid and the transfer of heat are dynamically changing. Through the imposition of periodic boundary conditions, the dynamic behavior in the fluid flow and heat transfer processes can be better captured, especially in cases where the physical quantities at the boundaries change periodically with time.
3. By presuming that the physical quantities at the boundaries have periodic variations, the discontinuity at the boundaries can be avoided, thereby reducing the error in numerical simulations.

The exact solution for u is given by

$$u(x, t) = 2\,\mathrm{sech}\,(3(-0.5 + \delta), \quad (x, t) \in \Omega, \tag{21}$$

$$\delta = \mathrm{mod}\left(x - x_0 + c \cdot t + \frac{L}{2}, L\right), \tag{22}$$

where L is the length of the spatial domain, $u \in (0.01\ \text{wt\%},\ 0.5\ \text{wt\%})$,

$c \in (0.8\ \text{m/s}, 1.2\ \text{m/s})$ and $L = x_{n+1} - x_n, x_0$ has an initial position of 0.5.

In this setup, the BIPINN model is a three-layer fully connected neural network, each layer contains 100 nodes with a Tanh activation function. The input consists of spatial coordinates x and time t, and the output is the predicted concentration u. The initial condition points are set to $N_u = 1{,}000$, boundary condition points to $N_b = 1{,}000$, and physical constraint points to $N_f = 1{,}000$.

The network's loss function is defined as

$$\text{Loss} = \text{MSE}_u + \text{MSE}_f + \text{MSE}_b. \tag{23}$$

MSE_u denotes the data loss, quantified as the mean squared error (MSE) between predicted and actual values.

$$\text{MSE}_u = \frac{1}{N_u}\sum_{i=1}^{N_u}(u_i - u_{\text{pred},i})^2. \tag{24}$$

Table 1: Comparison of PINN and BIPINN training results

Scheme	Epochs	Training time (s)	Error
PINN	4,000	382	10^{-5}
BIPINN	875	75	10^{-5}

MSE_f denotes the PDE loss, measured as the MSE of the PDE residual.

$$\mathrm{MSE}_f = \frac{1}{N_f}\sum_{j=1}^{N_f} f_j^2, \tag{25}$$

where $f_j = u_t - \mathrm{cu}_x = 0$.

MSE_b represents the boundary condition loss.

$$\mathrm{MSE}_b = \frac{1}{N_b}\sum_{k=1}^{N_b} (u_{b1,k} - u_{b2,k})^2, \tag{26}$$

where $u_{b1,k} = u(x_1, t_i)$ and $u_{b2,k} = u(x_2, t_i)$.

In this section, both PINN and BIPINN are employed to solve the convection-diffusion equation. The results show that the mean squared error (MSE) at the final epoch of model training is on the order of 10^{-5} (Table 1), indicating that the difference between the BIPINN solution and the reference solution is at a satisfactory and small level (Figure 4). Both methods perform well in solving this equation. We attribute this phenomenon to the simple, stable, and steady characteristics of the convection-diffusion system.

The total training duration of PINN amounts to 382 s, featuring 4,000 iterations, and the final value of the loss function is at the magnitude of 10^{-5}.

The total inference time of BIPINN is 75 s, with 875 iterations, and the final value of the loss function is likewise at the magnitude of 10^{-5}. (Comprehensive descriptions of the training workflow and experimental outcomes can be found in the Appendix.)

Further computations reveal that the training time demanded by BIPINN is reduced by 80.37% compared to PINN, and the computational resources required for each iteration have declined by 78.12% on a year-on-year basis.

Figure 4 shows the comparison of the reference solution, the neural network predicted solution, and the distribution of absolute error. Through the heatmap, it can be intuitively seen that the absolute error is small and evenly distributed, indicating that BIPINN performs well in solving PDEs. The predicted solution has a good match with the theoretical analytical solution, which shows that

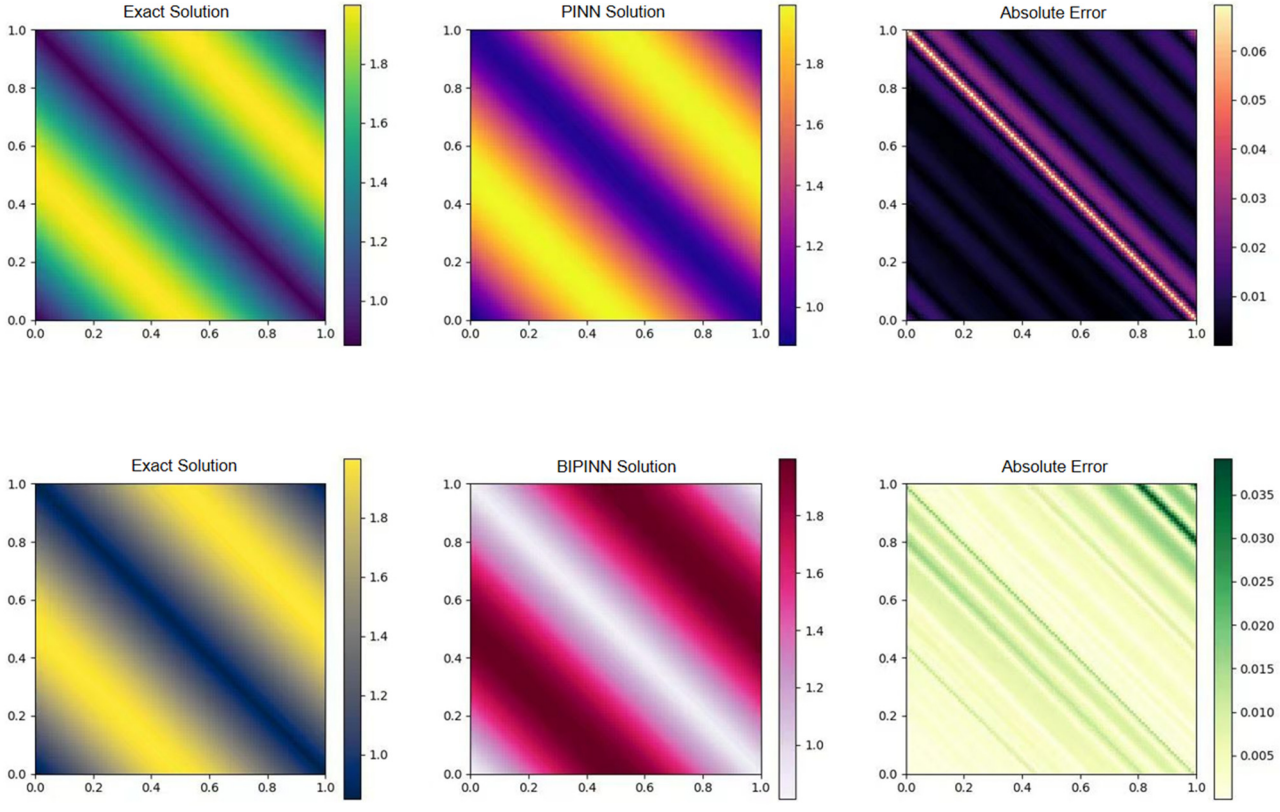

Figure 4: Heat maps of the (a) reference solution, (b) neural network predicted solution, and (c) distribution of absolute error.

it can better capture the convection-diffusion equation. Specifically,

1. The BIPINN can accurately capture the steep gradients of flow variables in convective diffusion of HNFs. This capability is attributed to its ability to handle complex nonlinear PDEs and incorporate physical law constraints to enhance prediction accuracy. Specifically, BIPINN embeds physical laws into the loss function, enabling it to automatically learn the complex dynamic behaviors of fluid flow and heat transfer, thereby accurately simulating the changes in temperature and concentration.
2. The cause of the absolute error is the significant noise generated by the variation in entropy generation during the convective process of the HNFs, which leads to an increase in the error between the prediction and the exact solution as the noise scale increases.
3. This phenomenon can be attributed to the distribution characteristics of Cu and Al_2O_3 nanoparticles in water. Due to their higher density and thermal diffusivity than water, they absorb more heat during the convective process, causing a decrease in the temperature of the surrounding water and forming a distinct temperature gradient, which is manifested as a steep change in flow variables.
4. Density difference: The density of Al_2O_3 and Cu nanoparticles is greater than that of water, making them more likely to aggregate and form local high-concentration regions in the fluid. This density difference causes the nanoparticles to tend to move along the flow lines during convection, thereby enhancing heat transfer.
5. Thermal diffusivity: The thermal diffusivity of nanoparticles is higher than that of water, meaning they can transfer heat to the surrounding fluid more quickly. This high thermal diffusivity enables nanoparticles to absorb and release heat more effectively during convection, thereby affecting the overall heat transfer efficiency.
6. Convection as an energy transfer method is usually irreversible. Heat is transferred from high-temperature regions to low-temperature regions through convection, and the total entropy of the system increases. In HNFs, this entropy generation phenomenon is particularly evident.
7. Heat transfer by nanoparticles: Nanoparticles absorb heat during convection and transfer it to the surrounding fluid. This process leads to local temperature changes and increases the entropy of the system. Specifically, nanoparticles absorb heat in high-temperature regions and release it in low-temperature regions as they move with the convection, raising the temperature of the surrounding fluid. This redistribution of heat increases the disorder of the system, manifested as an increase in entropy.
8. Irreversibility of convection: Heat transfer during convection is irreversible, meaning heat always flows from high-temperature regions to low-temperature regions. This irreversibility leads to an increase in the system's entropy, reflecting the energy loss in the heat transfer process. In HNFs, the presence of nanoparticles further intensifies this irreversibility, as they continuously absorb and release heat during convection, increasing the complexity of heat transfer and entropy generation.

5.2 Three-dimensional (3D) steady-state heat conduction with internal heat source

3D steady-state heat conduction with an internal heat source can be used to simulate the heat dissipation process of HNFs into the interior of electronic devices. In the 3D steady-state heat conduction problem for HNFs, internal heat sources impact the temperature distribution across the spatial domain. The steady-state heat conduction equation governs this temperature field, with the internal heat source term representing heat generation or absorption within the system. For two-dimensional steady-state conduction with an internal heat source, the equation is

$$\kappa_{\text{hnf}}\left(\frac{\partial^2 T}{\partial x^2}+\frac{\partial^2 T}{\partial y^2}\right)+q=\rho_{\text{hnf}}c_{\text{p,hnf}}\frac{\partial T}{\partial t}. \tag{27}$$

$T(x, y, t)$ denotes the temperature as a function of time t and spatial coordinates x and y, $(x, t) \in \Omega$.

q denotes the internal heat source term per unit volume, representing heat generation or absorption.

This study examines heat conduction in an Al_2O_3-Cu HNFs within a square domain containing an internal heat source. Assume a stable heat source with a constant boundary temperature of 1 along all edges of the square. The thermal conductivity κ_{hnf} varies within $\{\kappa_{\text{hnf}} \in R : 0.5 \leqslant \kappa_{\text{hnf}} \leqslant 1\}$, leading to a corresponding parameter θ variation. The range of θ is $\{\theta = q/\kappa_{\text{hnf}} \in R : 1 \leqslant \theta \leqslant 2\}$. The spatial coordinates and control parameter $\{x, y, \theta\}$ serve as the input for BIPINN.

Model training utilizes Monte Carlo sampling, with 3,000 boundary samples and 3,600 internal samples. BIPINN is structured with three hidden layers, each containing 100 neurons and using a sigmoid activation function. The loss function is

$$\text{Loss} = \text{MSE}_T + \text{MSE}_f + \text{MSE}_b, \tag{28}$$

where $\text{MSE}_T = \frac{1}{N_T}\sum_{i=1}^{N_T}(T_i - T_{\text{pred},i})^2$.

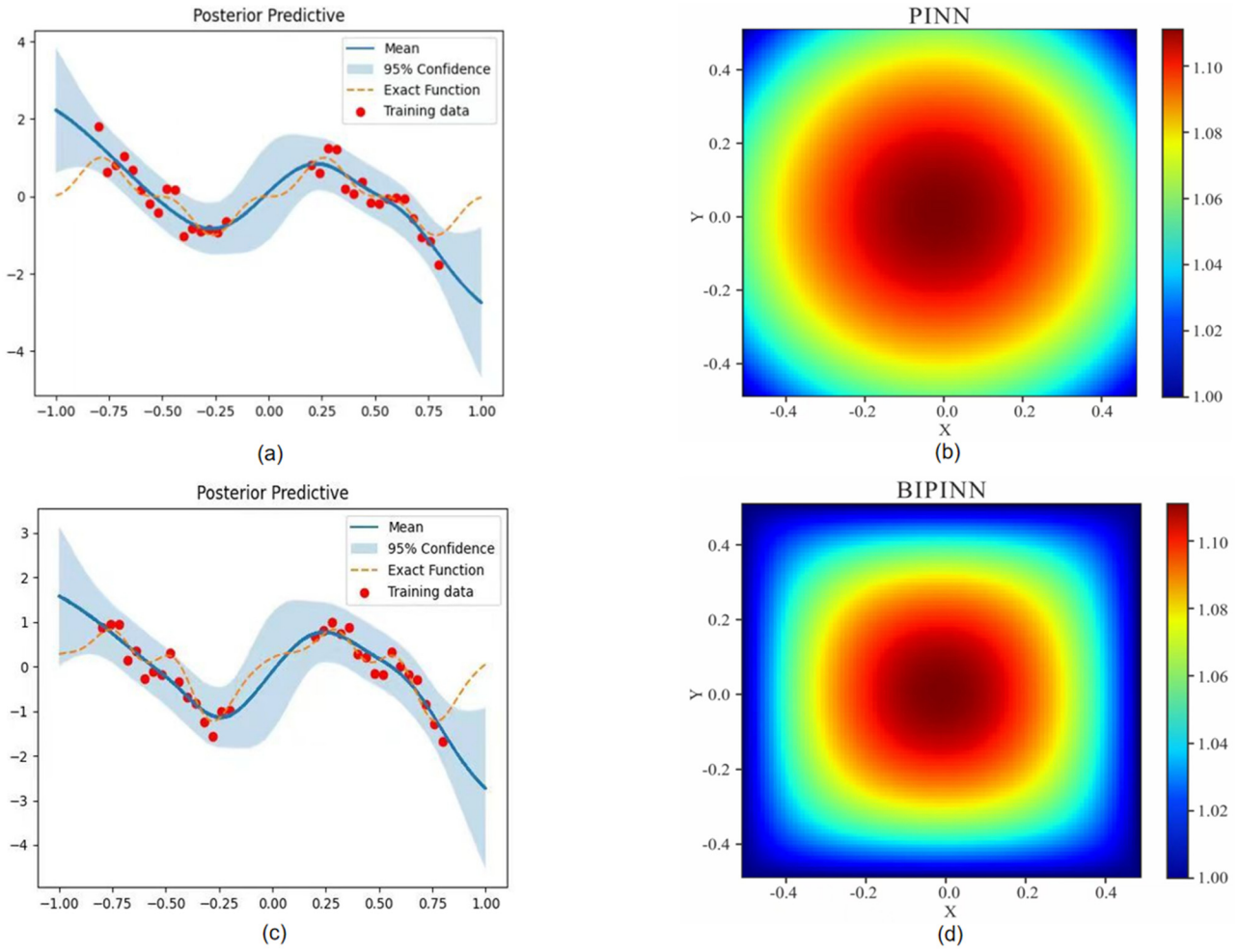

Figure 5: The comparison chart of prediction performance between PINN and BIPINN. (a) Heat flux predictions from the PINN model, (b) temperature field predictions from the PINN model, (c) heat flux predictions from the BIPINN model, and (d) temperature field predictions from the BIPINN model.

MSE_f and MSE_b are defined similarly to equations (25) and (26). The result is shown in Figure 5.

As depicted in Figure 5(a) and (c), the blue solid lines signify the average values of the heat flux predicted by the model, demonstrating the changing trend of the predicted heat flux at diverse spatial locations. In the heat conduction issue, Bayesian inference not only offers point estimations of the heat flux but also the 95% confidence interval of the posterior distribution of the heat flux obtained through MCMC sampling, clearly presenting the uncertainty range of the estimation outcomes. The width of the blue shaded area represents the level of uncertainty in the model's predictions. A wider shaded area indicates that the model has greater difficulty in accurately estimating the heat flux, which is due to the increased uncertainty from having less data available. The orange dashed line indicates the exact function, which is employed to validate the accuracy of the PINN model's prediction. The red dots denote the data points utilized for training the model, and the model endeavors to fit these data points to enhance the accuracy of the prediction. It can be observed from Figure 5(a) and (c) that the average predicted values of the improved BIPINN model (blue solid line) are proximate to the exact function (orange dashed line) in the majority of cases, and the fitting effect between the data points and the model is satisfactory.

As shown in Figure 5(b) and (d), both surrogate models constructed precisely captured the temperature variation trend. In contrast to PINN, the BIPINN surrogate model achieved a high-level accuracy. Further analysis indicated that under the same training points, PINN performed poorly in the boundary regions, whereas BIPINN maintained an excellent prediction performance in the boundary regions, thereby demonstrating that the improved BIPINN can adapt to the uncertainty of experimental data. That is, in the case of completely unknown boundary conditions, the invisible fluid

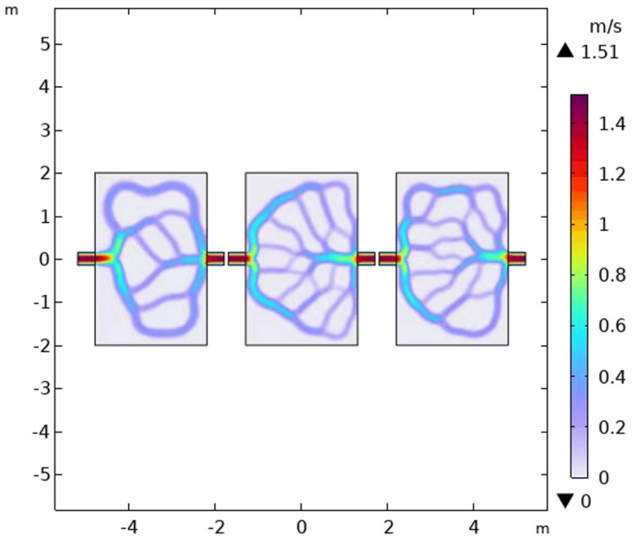

Figure 6: Cloud diagrams of velocity field distribution of liquid cooling channel cross-sections after different topology optimizations.

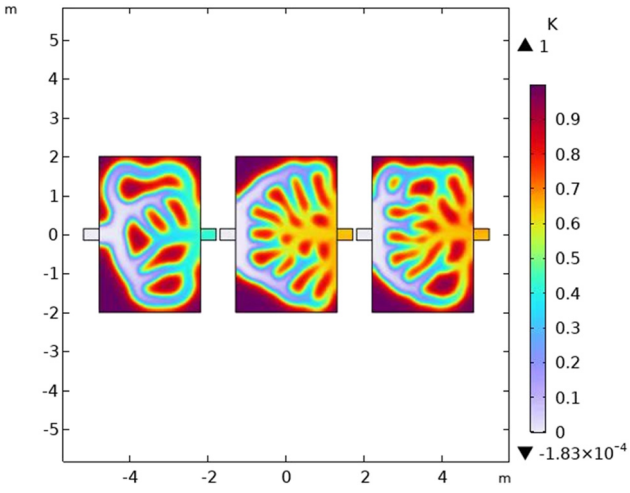

Figure 8: Cloud diagrams of temperature field distribution of liquid cooling channel cross-sections after different topology optimizations.

temperature field can be inferred based on sensor or environmental measurements *via* BIPINN.

Figure 5 also reveals the interaction mechanism between the internal heat source and the HNFs, specifically as follows:

(1) The presence of an internal heat source further complicates the heat conduction process. The internal heat source term represents the heat generation or consumption within the system, directly influencing the temperature distribution. We find that the addition of Al_2O_3-Cu nanoparticles gives the HNFs characteristics similar to those of a crystal at the microstructure level, resulting in a more pronounced effect of the temperature gradient within the fluid.

(2) The internal heat source term is spatially non-uniform, which makes the spatial variation of the temperature field more complex. In the HNFs, the high thermal conductivity of the nanoparticles (Al_2O_3 is approximately 30 W/m K, Cu is approximately 400 W/m K, and water is 0.6 W/m K) enables heat to be transferred more rapidly between the nanoparticles and the base fluid. This high thermal conductivity not only enhances the heat transfer efficiency but also allows the fluctuations in the temperature field to be smoothed out more quickly.

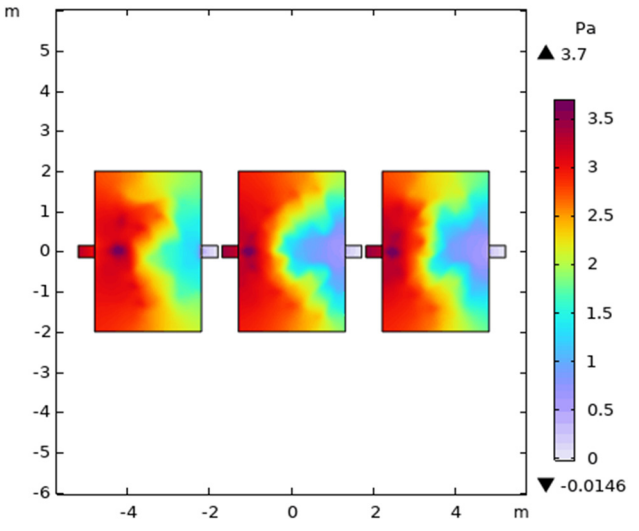

Figure 7: Cloud diagrams of pressure field distribution in cross-sections of liquid cooling channels after different topology optimizations.

Moreover, the numerical simulation results of a single heat source condition were analyzed utilizing the finite element method (COMSOL), and the analytical solution of COMSOL was compared with the predicted solution of BIPINN. Specifically, the velocity field distribution, pressure field distribution, and temperature field distribution of the topologically optimized liquid cooling channel cross-section obtained from COMSOL were employed (Figures 6–8).

Figure 7 shows the pressure field distribution of the liquid-cooled channel cross-sections after different topology optimizations when the Reynolds number Re = 150. It can be seen from the figure that the fluid pressure distribution within the topology-optimized channels is uneven. The highest velocity occurs at the inlet and outlet corners, corresponding to the maximum pressure. The pressure in the horizontal parallel channels in the middle area decreases from left to right. This is because when the fluid flows through the corners, local vortices are generated. After topology optimization, the flow velocity within the channels is lower, and the cooling medium is relatively evenly distributed among the channels in all directions.

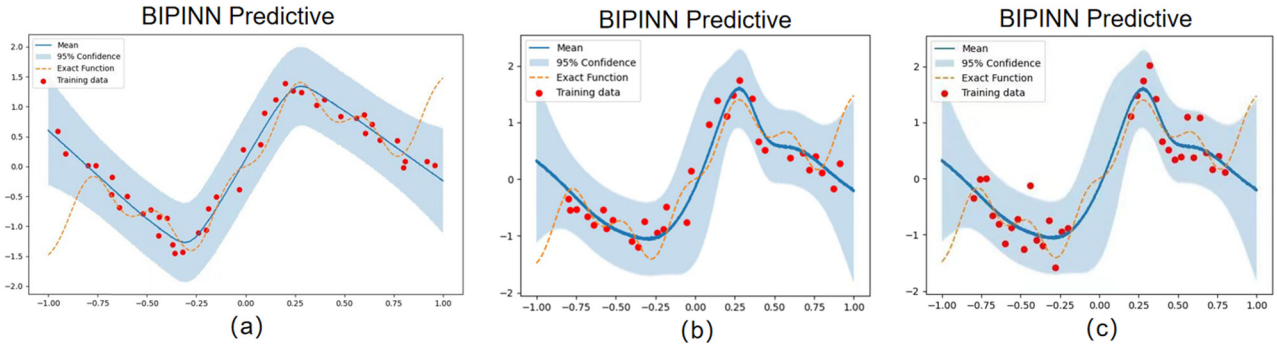

Figure 9: (a–c) The multi-physics prediction results of BIPINN.

Figure 8 presents the temperature field distribution of the liquid cooling channel cross-sections after diverse topology optimizations under the single heat source condition with a heating power of 200 W. It can be observed from the figure that the fluid temperature in the peripheral channels is relatively low, while that in the middle horizontally arranged channels is relatively high. This is because, as depicted in Figure 6, the flow velocity in the converging channels is faster, resulting in more heat being carried away per unit time compared to the parallel channels in the diverging region. Hence, the maximum temperature emerges in the middle area. Regarding the topology-optimized channels, the fluid temperature gradually rises from the inlet to the outlet side. The fluid temperature in the middle horizontally arranged channels is relatively uniform. This is because after the fluid flows in from the inlet, a greater flow rate is allocated to the vertical channels on the left, thereby being distributed to the middle horizontally arranged channels.

We also adjusted the computational framework to predict the multi-physics involved in the heat channels of the HNFs after topological optimization. The result is shown in Figure 9. (Comprehensive descriptions of the training workflow and experimental outcomes can be found in the Appendix.)

Figure 9(a) and (b) shows the prediction results of BIPINN under the multi-physics field effect, highlighting the consistency between the two methods and further confirming the effectiveness of BIPINN in evaluating different microstructures.

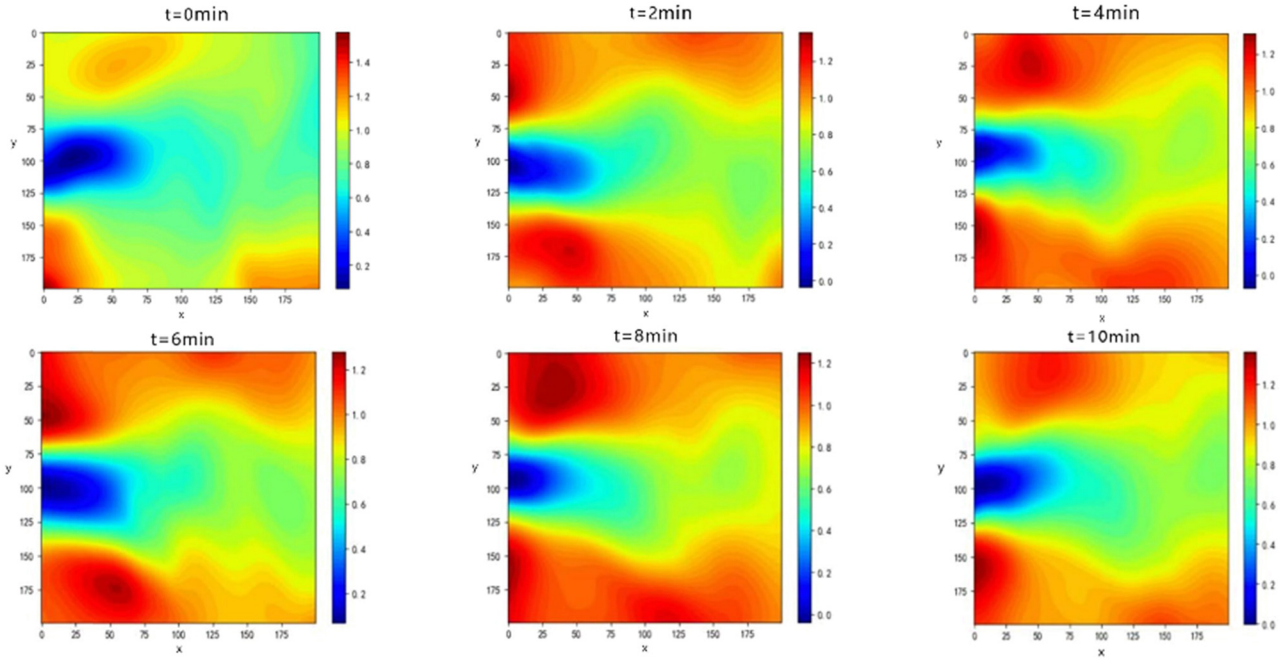

Figure 10: 3D unsteady heat conduction in HNFs simulated by BIPINN.

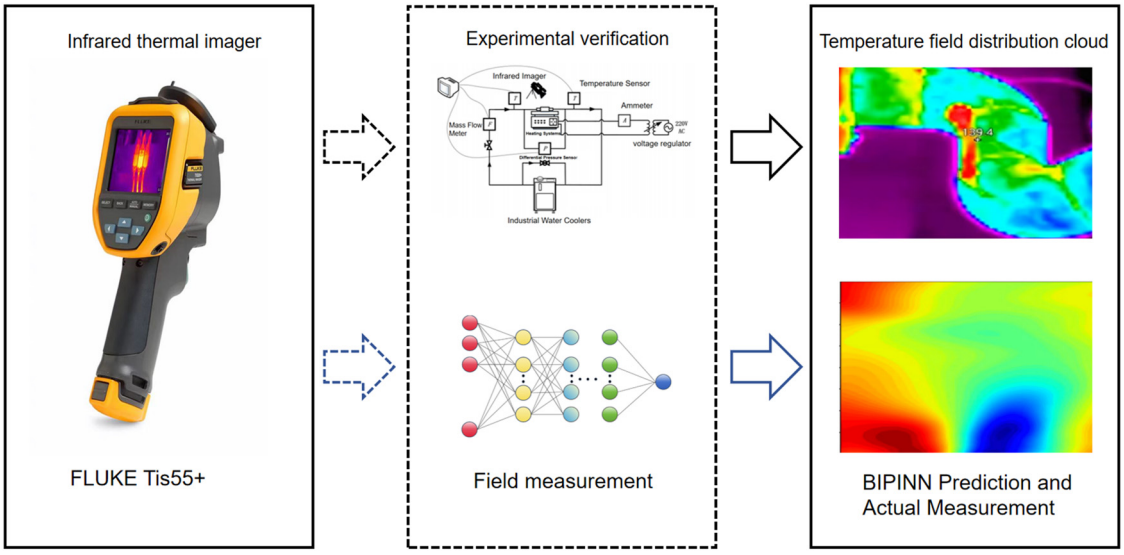

Figure 11: The results of infrared imaging and BIPINN network prediction.

Figure 9(c) shows that BIPINN has difficulty accurately describing these complex physical processes simultaneously, leading to poor prediction performance in complex topological channels. The specific reasons can be classified as follows:

(1) The model is overly complex, leading to overfitting, especially when the training data are limited. The model may overfit the noise in the training data and fail to generalize to new data.
(2) The boundary conditions and initial conditions of complex thermal channels are very complex. These conditions have not been accurately embedded into the model, resulting in fitting failure.
(3) Topology optimization increases the complexity of thermal channels. Complex thermal channels involve the coupling of multiple physical phenomena such as fluid flow and heat transfer. In the flow and heat transfer of HNFs, flow and heat transfer are coupled. The flow state affects heat transfer, and the heat distribution in turn affects the flow. For example, when the fluid temperature rises, its density may decrease, causing buoyancy force and changing the flow pattern, while the flow also changes the distribution of the temperature field.

5.3 3D unsteady heat conduction

In 3D unsteady heat conduction, HNF can be used as heat dissipation working media in liquid cooling circulation systems, which can provide excellent heat dissipation performance for pipes, valves, engine components, *etc*. The

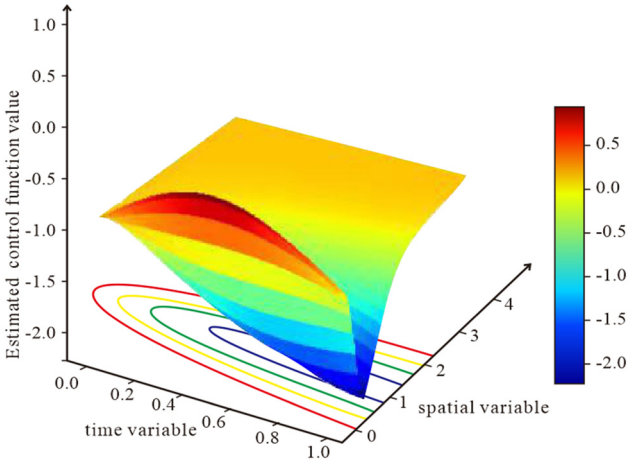

Figure 12: BIPINN model for dynamic heat control functions in HNFs.

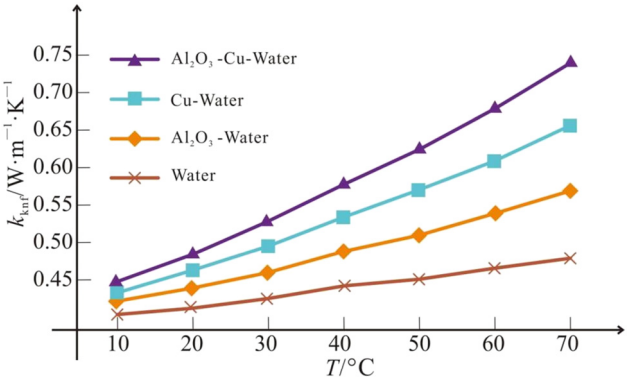

Figure 13: Variation in the thermal conductivity of NFs with temperature.

heat conduction control equation governs temperature changes over time and space, incorporating terms for conduction, convection, and internal heat sources. The unsteady heat conduction equation for HNFs is given by

$$\rho c_{\mathrm{p}}\frac{\partial T}{\partial t} + \rho c_{\mathrm{p}}\left(u\frac{\partial T}{\partial x} + v\frac{\partial T}{\partial y}\right) = \kappa_{\mathrm{hnf}}\left(\frac{\partial^2 T}{\partial x^2} + \frac{\partial^2 T}{\partial y^2}\right) + q, \quad (29)$$

where u and v are the velocity components in the x and y directions, respectively.

q is the volumetric heat source term, indicating heat generation per unit volume. It is approximated by a complete cubic polynomial, $q \in [0, 1]$.

The conduction term $\kappa_{\mathrm{hnf}}\left(\frac{\partial^2 T}{\partial x^2} + \frac{\partial^2 T}{\partial y^2}\right)$ represents spatial diffusion and conduction within the temperature field. It is proportional to the temperature gradient $\left(\frac{\partial^2 T}{\partial x^2} + \frac{\partial^2 T}{\partial y^2}\right)$ and thermal conductivity κ, demonstrating heat transfer in the nanofluid.

The source term $\left(u\frac{\partial T}{\partial x} + v\frac{\partial T}{\partial y}\right)$ accounts for spatial and temporal heat sources, either externally applied or resulting from other thermal exchange processes.

This equation models a dynamic heat conduction process, where the temperature field changes over time and space due to conduction, external heat sources, and fluid thermal properties. These problems are supported by specific boundary conditions, classified as follows:

$$\begin{aligned} T(\mathbf{x}, t) &\rightarrow \bar{T}(\mathbf{x}, t), \mathbf{x} \in \Gamma_1 \\ -k\frac{\partial T(\mathbf{x}, t)}{\partial \mathbf{n}} &= \bar{q}(\mathbf{x}, t), \quad \mathbf{x} \in \Gamma_2, \end{aligned} \quad (30)$$

where $\Gamma_1 \cap \Gamma_2 = \varnothing; \Gamma_1 \cup \Gamma_2 = \Gamma; \Gamma_1, \Gamma_2 \in \partial\Omega$.

The first boundary condition is the Dirichlet boundary condition. It specifies that the temperature on boundary Γ_1, T, is set as a function of the given $\bar{T}(x, t)$, and specifies the value of the temperature at the boundary.

The second boundary condition is the Neumann boundary condition. It specifies that the heat flux density on boundary Γ_2 (defined as the derivative along the normal vector, scaled by thermal conductivity) matches a given function $\bar{q}(\mathbf{x}, t)$, where n represents the outward normal vector on the boundary.

In 3D unsteady heat conduction problems, combining Dirichlet and Neumann conditions allows BIPINN to predict the dynamic heat flux distribution in HNFs using minimal boundary data. Since fluid heat transfer adheres to the conservation of energy, changes in boundary temperature must correspond with shifts in internal energy distribution. To model this relationship, we randomly select 400 sample points on the temperature boundary and 300 on the heat flux boundary. Sampling times for these conditions span the interval $t_i = t_0 + i\Delta t$, with a time step Δt = 10s, beginning at $t_0 = 0$. Additionally, 5,486 nodes are randomly sampled across the domain as training points. These training points enable dynamic adjustment of the weights for each component in the loss function, optimizing the training process and outcomes. The result is shown in Figure 10. The loss function components are structured as follows:

$$W\mathrm{loss} = W_{\mathrm{F}}\mathrm{loss}_{\mathrm{F}} + W_{\mathrm{N}}\mathrm{loss}_{\mathrm{BCq}} + W_{\mathrm{U}}(\mathrm{loss}_{\mathrm{BCT}} + \mathrm{loss}_{\mathrm{RC}}). \quad (31)$$

W_{F}, W_{U}, and W_N are the weight coefficients. (Comprehensive descriptions of the training workflow and experimental outcomes can be found in the Appendix.)

1) $\mathrm{loss}_{\mathrm{F}}$:

$$\mathcal{L}_{\mathrm{PDE}} = \frac{1}{N_{\mathrm{res}}}\sum_{i=1}^{N_{\mathrm{res}}}\left(\rho c_{\mathrm{p}}\frac{\partial T}{\partial t} + \rho c_{\mathrm{p}}\left(u\frac{\partial T}{\partial x} + v\frac{\partial T}{\partial y}\right) - \kappa_{\mathrm{hnf}}\left(\frac{\partial^2 T}{\partial x^2} + \frac{\partial^2 T}{\partial y^2}\right) - q\right)^2 \quad (32)$$

MSE of residuals for the governing equation. N_{res} is the number of training points used to compute the PDE residuals.

2) $\mathrm{loss}_{\mathrm{BCq}}$:

$$\begin{aligned} \mathcal{L}_{\mathrm{BC}} &= \frac{1}{N_{\mathrm{vbc}}}\sum_{i=1}^{N_{\mathrm{bc}}}(\mathbf{u}(x, y, z, t) - 0)^2 \\ &\quad + \frac{1}{N_{\mathrm{vbc}}}\sum_{j=1}^{N_{\mathrm{bc}}}(\mathbf{u}(x_i, y_i, z_i, t_i) - \mathbf{U}_\infty)^2 \\ \mathcal{L}_{\mathrm{BC}} &= \frac{1}{N_{\mathrm{vbc}}}\sum_{i=1}^{N_{\mathrm{bc}}}(\mathbf{v}(x, y, z, t) - 0)^2 \\ &\quad + \frac{1}{N_{\mathrm{vbc}}}\sum_{j=1}^{N_{\mathrm{bc}}}(\mathbf{v}(x_i, y_i, z_i, t_i) - \mathbf{U}_\infty)^2. \end{aligned} \quad (33)$$

MSE of residuals for the boundary velocity. ($i \in$ wall, $j \in$ free − stream)

3) $\mathrm{loss}_{\mathrm{BCT}}$ and $\mathrm{loss}_{\mathrm{RC}}$: Sum of squared residuals for boundary temperature and initial temperature points, respectively

$\mathrm{loss}_{\mathrm{BCT}}$:

$$\mathcal{L}_{\mathrm{IC}} = \frac{1}{N_{ic}}\sum_{i=1}^{N_{ic}}(T_{\mathrm{pred}}(x_i, y_i, z_i, t_i) - T_{\mathrm{initial}}(x_i, y_i, z_i, t_i))^2. \quad (34)$$

$\mathrm{loss}_{\mathrm{RC}}$:

$$\mathcal{L}_{\mathrm{flux}} = \frac{1}{N_{\mathrm{flux}}}\sum_{i=1}^{N_{\mathrm{flux}}}\left(-k\frac{\partial T_{\mathrm{pred}}}{\partial n}(x_i, y_i, z_i, t_i) - q_{\mathrm{initial}}(x_i, y_i, z_i, t_i)\right)^2 \quad (35)$$

As shown in Figure 10,

(1) BIPINN can accurately simulate the dynamic behavior of HNFs at different time steps. By embedding physical laws into the loss function, BIPINN can automatically learn the complex dynamic behavior in the heat conduction process, thereby providing high-precision prediction results. Specifically, BIPINN can capture the evolution of the temperature field over time and space, demonstrating its dynamic behavior at different time steps.
(2) In unsteady heat conduction problems, the variation in boundary conditions has a particularly significant impact on the temperature field. The model's advantage lies in its ability to handle complex boundary conditions and irregular geometries. By combining Dirichlet and Neumann boundary conditions, it can achieve high accuracy and low-cost predictions with a relatively small amount of boundary data.

To further explore and verify the thermal properties of 3D unsteady-state heat conduction, we set up a liquid cooling circulation experimental system and compared it with the temperature field distribution predicted by BIPINN. (Comprehensive descriptions of the training workflow and experimental outcomes can be found in the Appendix.) The result is shown in Figure 11.

According to the aforementioned experimental scheme and simulation method, when the uniformly distributed heat source heating power is 200 W, it can be seen from the figure that the simulation results of the experiment show a good match in the temperature field distribution trend, and the following conclusions can be drawn:

1) The highest temperature in the channel occurs at the corner on the inlet side, which is the side with low flow velocity. It verified the conversion of kinetic energy into internal energy by differing fluid stresses. Loss of temperature from the surface to the fluid flow is possible
2) The maximum temperature on the upper surface of the liquid cooling plate decreases with the increase in flow rate, and the decreasing trend gradually slows down. This is because as the flow rate increases, the influence of convective heat transfer on the overall heat dissipation performance gradually becomes larger compared to solid heat conduction.
3) The comparison results show that the temperature field results predicted by BIPINN are generally in good agreement with the experimental measurements. BIPINN can better capture the heat transfer flow. However, near the vortex, the error is still relatively large. The physical quantities in these areas change more complexly, indicating that BIPINN still needs improvement in handling complex problems, which is also the focus of future research. In conclusion, there is a good consistency between the physical field predicted by BIPINN and the actual observed results, indicating that it can be used as an alternative model for solving similar problems.

5.4 Exact controllability of the fluctuation equation with complex boundary conditions

This study focuses on controlling temperature fluctuations in HNFs over time. By adjusting boundary conditions or internal source terms, we aim to reach a fully stationary or stable state within a finite period, achieving "exact controllability to zero." In industrial processes, many devices require precise temperature control, such as chemical reactors, metallurgical furnaces, and glass manufacturing equipment. The temperature control of these devices often involves complex boundary conditions and dynamic heat sources, necessitating precise control strategies to ensure process stability and product quality. To manage the complex optimization and numerical challenges, especially for nonlinear or ill-posed systems, we introduce a variable control function. The one-dimensional heat equation with a complex boundary is as follows:

$$\begin{cases} y_t - y_{xx} = \Psi_\omega u(y - \alpha(x,t)), & (x,t) \in Q_T^{\mathcal{L}} \\ y(0,t) = 0, & t \in (0,T) \\ y(x,0) = \sin(\pi x), & x \in (0,S_0) \\ y(\mathcal{L}(t),t) = 0, & \\ \mathcal{L}(0) = S_0, & \end{cases} \tag{36}$$

The initial fluctuation is set to zero. $S_0 > 0$, $0 < a < b < S_0$, and $\omega = (a,b)$, $\mathcal{L} \in C^1([0,T])$ *i*th $\mathcal{L}(t) > 0$, we set $Q_T^{\mathcal{L}} \coloneqq \{(x,t);\ x \in (0,\mathcal{L}(t)), t \in (0,T)\}$, Ψ_ω is the characteristic function.

$u \in S^\infty(Q_T^{\mathcal{L}})$ denotes the control input, supported by subdomain ω, which influences the reaction rate of the process described in (31). This reflects the decay estimates of the state S^∞ norm for the uncontrolled system with a complex boundary, allowing the state to approach the vicinity of its residual state.

$\alpha \in S^\infty(\mathbb{R} \times \mathbb{R}^+)$ and $(\mathcal{L}, y)$ relate to a complex boundary, a section of the domain boundary that is unknown *a priori*. An additional condition is applied

$$\mathcal{L}'(t) = -y_x(\mathcal{L}(t),t), t \in (0,T), \tag{37}$$

to ensure well-posedness for $(\mathcal{L}, y)$.

In addressing the complex boundary problem, we often encounter PDEs involving convection and heat

conduction, complicating exact controllability to zero. These problems usually entail an infinite-dimensional state space instead of a finite-dimensional state vector. To overcome this, we apply BIPINN, which integrates DL with physical laws to estimate the control and system state, solving for a control function that ensures exact controllability to zero in equation (36). The objective of the fluctuation control problem is to achieve complete rest or a stable state of the system within a finite time by adjusting the boundary conditions or internal source terms of the system, that is, to achieve "zero controllability." The result is shown in Figure 12.

In HNFs, this process involves complex physical mechanisms.

1) Fluctuations in the temperature field: Fluctuations in the temperature field are caused by changes in the heat source term and boundary conditions. Under non-steady-state conditions, the changes in the temperature field are more complex and require control functions to regulate these fluctuations.
2) Complex boundary conditions (such as free boundaries) make the fluctuation control problem more complicated. Changes in boundary conditions directly affect the distribution of the temperature field, so precise control functions are needed to achieve zero controllability.

As shown in Figure 12,

1) The 3D surface plot clearly shows the fluctuation of the solution values within a specific spatiotemporal range, where red represents high-value regions and blue represents low-value regions, thereby intuitively presenting the distribution characteristics of the BIPINN solution. This method not only solves high-dimensional and nonlinear PDE problems but also enables precise control of the target by adjusting the boundary conditions or internal source terms of the system.
2) Regularization Mechanism: Without regularization, the model would adopt high-order fitting to train data. However, with the addition of regularization, the model tends to choose a more reasonable order, solving high-dimensional and nonlinear PDE problems. Regularization restricts the complexity of the model, preventing it from overly relying on specific details in the training data during the training process and instead learning more generalized rules. By penalizing predictions that exceed the range through regularization terms, the model is guided to learn solutions that conform to prior knowledge.

Table 2: Measured thermal conductivity values

T / °C	κ (W m^{-1} K^{-1})			
	φ = 0.0125	φ = 0.025	φ = 0.1	φ = 0.2
10	0.4830	0.4846	0.4890	0.4925
20	0.5019	0.5040	0.5062	0.5120
30	0.5192	0.5210	0.5241	0.5293
40	0.6360	0.6382	0.6400	0.6445
45	0.6426	0.6423	0.6492	0.6552
50	0.6502	0.6513	0.6504	0.6590
55	0.6547	0.6571	0.6577	0.6630
60	0.6600	0.6620	0.6558	0.6700
65	0.6643	0.6870	0.7007	0.7151

6 Sensitivity analysis

In this study, various volume concentrations of Al_2O_3-Cu/water HNFs were prepared according to the study by Suresh *et al.* [62]. A sensitivity analysis experiment was set up, and the experimental results are presented in Table 2.

A comparison was made between the thermal conductivity values that were obtained *via* experimental study and the reference values of water that had not been polluted with any pollutants. The thermal conductivity values were found to be greater than those of pure water in each of the five volumetric concentrations that were tested. The results of the experiment demonstrated that an increase in the temperature was accompanied by an increase in the thermal conductivity values of the hybrid nanofluid. This was seen despite the fact that the temperature was rising. An increase in temperature induces an increase in the molecular movements in the hybrid nanofluid, which in turn causes a significant increase in the rate at which heat is exchanged among the molecules.

This cycle continues until the temperature is decreased. A rise in the collision speed between the particles is brought about by the Brownian motion, which in turn brings about an increase in the thermal conductivity of the HNFs.

The temperature gradient sensitivity analysis was conducted on 0.1% Al_2O_3-Cu/water HNFs, and the results are shown in Figure 13.

As shown in Figure 13, the thermal conductivity of the HNFs with Al_2O_3-Cu nanoparticles added to water as the base liquid continuously increases with the rise in temperature, demonstrating its sensitivity to temperature gradient changes.

The thermal conductivity of the Al_2O_3-Cu HNFs increases with temperature, demonstrating excellent heat dissipation characteristics. A maximum of 52.62% enhancement was observed in the thermal conductivity by Al_2O_3-Cu HNFs.

Experimentally, smaller Cu particles occupy spaces between larger Al_2O_3 particles, forming a "large particle-small particle-base fluid molecule" structure that enhances heat transfer efficiency in the nanofluid.

7 Conclusion

In this work, we presented a unified computing framework for the examination of the momentum and heat-transfer mechanisms of Al_2O_3–Cu/water HNFs. The framework consists of an analytical methodology that utilizes the K–L expansion first to extract a reduced-order representation from the time-dependent data including heat transfer and flow data. The reduced-order data are then used to inform a PINN under Bayesian inference (BIPINN) that solves the governing PDEs in a complex physical domain. The methodology described captures complex temperature distributions and flow characteristics of HNFs while requiring a minimal amount of data with respect to available measurements and inaccuracies. The framework and associated methodology were assessed in a variety of situations that collectively demonstrated the robustness and flexibility of the computational framework from a performance perspective, including (i) free-boundary null controllability of the one-dimensional heat equation, (ii) two-dimensional unsteady convection–diffusion, (iii) 3D steady-state heat conduction with internal heat generation, and (iv) 3D unsteady thermal conduction over time. In all dimensional characteristics and boundary conditions presented, the model displayed strong predictive capability and simulation performance.

In short, the framework technology integrates the K–L expansion, BIPINN, and surrogate modeling into a coherent and efficient method. As demonstrated in our comparative studies, BIPINN reduced training time by approximately 80.37% and reduced computing resources by approximately 78.12% as compared to traditional PINNs realization. In conclusion, even with less data and lesser computational time, we maintained similar results compared to both COMSOL finite element simulations of the same problem and coincided with experimental measurements. This illustrates that the framework can practically perform well and offer helpful conclusions in understanding how to apply data science and AI-based modeling to thermal-fluid systems for engineering design.

Acknowledgments: The authors acknowledge the support and funding by the Key Laboratory of Key Strike and Precision Destruction, Liaoning Province, China. The authors acknowledge the support and funding by the China Central Guiding Fund for Local Science and Technology Development (grant number 1080009000401).

Funding information: The authors acknowledge the support and funding by the Key Laboratory of Key Strike and Precision Destruction, Liaoning Province, China. The authors acknowledge the support and funding by the China Central Guiding Fund for Local Science and Technology Development (grant number 1080009000401).

Author contributions: Ende Wang designed the experiments and Chenming Zhao carried them out. Qingquan Liu developed the model code and performed the simulations. Mingming Du prepared the manuscript with contributions from all co-authors. All authors have accepted responsibility for the entire content of this manuscript and approved its submission.

Conflict of interest: The authors state no conflict of interest.

Data availability statement: The datasets generated and/or analyzed during the current study are available from the corresponding author on reasonable request.

References

[1] Emmerich T, Ronceray N, Agrawal KV, Garaj S, Kumar M, Noy A, et al. Nanofluidics. Nat Rev Methods Primers. 2024;4(1):69. doi: 10.1038/s43586-024-00344-0.

[2] Siricharoenpanich A, Wiriyasart S, Naphon P. Study on the thermal dissipation performance of GPU cooling system with nanofluid as coolant. Case Stud Therm Eng. 2021;25:100904. doi: 10.1016/j.csite.2021.100904.

[3] Zhang L, Tian L, Jing Y, Qu P, Zhang A. Molecular dynamics study on the mechanism of nanofluid coolant's thermal conductivity improvement. J Mol Liq. 2022;345:118228. doi: 10.1016/j.molliq.2021.118228.

[4] Cimpean DS, Sheremet MA, Pop I. Mixed convection of hybrid nanofluid in a porous trapezoidal chamber. Int Commun Heat Mass Transf. 2020;116:104627. doi: 10.1016/j.icheatmasstransfer.2020.104627.

[5] Rashid FL, Aljibori HS, Mohammed HI, Ameen A, Ahmad S, Ben Hamida MB, et al. Recent advances and developments of the application of hybrid nanofluids in parabolic solar collector energy systems and guidelines for future prospects. J Eng Res. 2024. doi: 10.1016/j.jer.2024.04.023.

[6] Rashed AS, Nasr E, Mabrouk SM. Bioconvective flow surrounding a thin surgical needle in blood incorporating ternary hybrid nanoparticles. J Comput Methods Differ Equ. 2024;1–27. doi: 10.22034/cmde.2024.61425.2643.

[7] Shah SZH, Ayub A, Bhatti S, Khan U, Ishak A, Sherif EM, et al. Aspects of inclined magnetohydrodynamics and heat transfer in a non-Newtonian trihybrid bionanofluid flow past a wedge-shaped

artery utilizing artificial neural network scheme. J ZAMM - J Appl Math Mech/Zeitschrift für Angewandte Mathematik und Mechanik. 2024;104(12):e202400278. doi: 10.1002/zamm.202400278.

[8] Suresh S, Venkitaraj KP, Selvakumar P, Chandrasekar M. Synthesis of Al_2O_3–Cu/water hybrid nanofluids using two step method and its thermo physical properties. Colloids Surf A: Physicochem Eng Asp. 2011;388(1):41–8. doi: 10.1016/j.colsurfa.2011.08.005.

[9] Hemmat Esfe M, Toghraie D, Alidoust S, Amoozadkhalili F, Mohammadnejad Ardeshiri E. Investigating the rheological behavior of a hybrid nanofluid (HNF) to present to the industry. Heliyon. 2022;8(12):e11561. doi: 10.1016/j.heliyon.2022.e11561.

[10] Venkateswarlu B, Chavan S, Joo SW, Kim SC. Impact of hybrid nanofluids on thermal management of cylindrical battery modules: A numerical study. J Energy Storage. 2024;99:113266. doi: 10.1016/j.est.2024.113266.

[11] Khalil S, Abbas T, Nawaz R. Enhanced thermal and flow behavior of Cu-Al_2O_3/water hybrid nanofluids in porous media under variable magnetic field conditions. Int J Thermofluids. 2025;27:101166. doi: 10.1016/j.ijft.2025.101166.

[12] Khashi'ie NS, Arifin NM, Sheremet M, Pop I. Shape factor effect of radiative Cu–Al_2O_3/H_2O hybrid nanofluid flow towards an EMHD plate. Case Stud Therm Eng. 2021;26:101199. doi: 10.1016/j.csite.2021.101199.

[13] Tiam Kapen P, Gervais Njingang Ketchate C, Fokwa D, Tchuen G. Linear stability analysis of (Cu-Al_2O_3)/water hybrid nanofluid flow in porous media in presence of hydromagnetic, small suction and injection effects. Alex Eng J. 2021;60(1):1525–36. doi: 10.1016/j.aej.2020.11.007.

[14] Ayub A, Hussain Shah SZ, Iqbal Z, Selmi R, Aljohani AF, Alharthi AM, et al. Streamlines and neural intelligent scheme for thermal transport to infinite shear rate for ternary hybrid nanofluid subject to homogeneous-heterogeneous reactions. Case Stud Therm Eng. 2024;61:104961. doi: 10.1016/j.csite.2024.104961.

[15] Ayub A, Shah SZH, Sirisubtawee S. Multifactorial analysis of ternary magnetized radiative nanofluid with waste discharge concentration and microorganism behavior: Multi-hidden layer mechanism. Nano. 2025;20:32. doi: 10.1142/S1793292025500031.

[16] Yoon JW, Kumar A, Kumar P, Hippalgaonkar K, Senthilnath J, Chellappan V. Explainable machine learning to enable high-throughput electrical conductivity optimization and discovery of doped conjugated polymers. Knowl Syst. 2024;295:111812. doi: 10.1016/j.knosys.2024.111812.

[17] Akbar SS, Mustafa M, Mushtaq A. Exploring integrated heat and mass transfer in von-Kármán dynamics involving Reiner-Rivlin fluid with regression models. Case Stud Therm Eng. 2024;62:105154. doi: 10.1016/j.csite.2024.105154.

[18] Guo L, Zhang Y, Li X, Wang Z, Liu Y, Bai L, et al. Data-driven power flow calculation method: A lifting dimension linear regression approach. IEEE Trans Power Syst. 2022;37(3):1798–808. doi: 10.1109/TPWRS.2021.3112461.

[19] Hwangbo S, Al R, Sin G. An integrated framework for plant data-driven process modeling using deep-learning with Monte-Carlo simulations. Computers Chem Eng. 2020;143:107071. doi: 10.1016/j.compchemeng.2020.107071.

[20] Kanti P, Sharma KV, Jamei M, Kumar HGP. Thermal performance of hybrid fly ash and copper nanofluid in various mixture ratios: Experimental investigation and application of a modern ensemble machine learning approach. Int Commun Heat Mass Transf. 2021;129:105731. doi: 10.1016/j.icheatmasstransfer.2021.105731.

[21] Marulasiddeshi HB, Kanti PK, Jamei M, Prakash SB, Sridhara SN, Said Z. Experimental study on the thermal properties ofAl2O3-CuO/water hybrid nanofluids: Development of an artificial intelligence model. Int J Energy Res. 2022;46(15):21066–83. doi: 10.1002/er.8739.

[22] Kanti PK, Sharma P, Koneru B, Banerjee P, Jayan KD. Thermophysical profile of graphene oxide and MXene hybrid nanofluids for sustainable energy applications: Model prediction with a Bayesian optimized neural network with K-cross fold validation. FlatChem. 2023;39:100501. doi: 10.1016/j.flatc.2023.100501.

[23] Hossain R, Azad AK, Hasan MJ, Rahman MM. Radiation effect on unsteady MHD mixed convection of kerosene oil-based CNT nanofluid using finite element analysis. Alex Eng J. 2022;61(11):8525–43. doi: 10.1016/j.aej.2022.02.005.

[24] Hanif H. A finite difference method to analyze heat and mass transfer in kerosene based γ-oxide nanofluid for cooling applications. Phys Scr. 2021;96:095215. doi: 10.1088/1402-4896/ac098a.

[25] Akbar NS, Zamir T, Akram J, Noor T, Muhammad T. Simulation of hybrid boiling nano fluid flow with convective boundary conditions through a porous stretching sheet through Levenberg Marquardt artificial neural networks approach. Int J Heat Mass Transf. 2024;228:125615. doi: 10.1016/j.ijheatmasstransfer.2024.125615.

[26] Alghamdi M, Akbar NS, Zamir T, Muhammad T. Double layered combined convective heated flow of Eyring-Powell fluid across an elevated stretched cylinder using intelligent computing approach. Case Stud Therm Eng. 2024;54:104009. doi: 10.1016/j.csite.2024.104009.

[27] Shah FA, Zamir T, Akbar NS, Mikhaylov A. Levenberg-Marquardt design for analysis of maxwell fluid flow on ternary hybrid nanoparticles passing over a Riga plate under convective boundary conditions. Results Eng. 2024;24:103502. doi: 10.1016/j.rineng.2024.103502.

[28] Xu T, Liu D, Hao P, Wang B. Variational operator learning: A unified paradigm marrying training neural operators and solving partial differential equations. J Mech Phys Solids. 2024;190:105714. doi: 10.1016/j.jmps.2024.105714.

[29] Bertrand F, Boffi D, Halim A. Data-driven reduced order modeling for parametric PDE eigenvalue problems using Gaussian process regression. J Comput Phys. 2023;495:112503. doi: 10.1016/j.jcp.2023.112503.

[30] Lu L, Meng X, Mao Z, Karniadakis GE. DeepXDE: A deep learning library for solving differential equations. SIAM Rev. 2021;63(1):208–28. doi: 10.1137/19M1274067.

[31] Mishra S, Molinaro R. Estimates on the generalization error of physics-informed neural networks for approximating PDEs. IMA J Numer Anal. 2023;43(1):1–43. doi: 10.1093/imanum/drab093.

[32] Yu J, Lu L, Meng X, Karniadakis GE. Gradient-enhanced physics-informed neural networks for forward and inverse PDE problems. Computer Methods Appl Mech Eng. 2022;393:114823. doi: 10.1016/j.cma.2022.114823.

[33] Lorenzen F, Zargaran A, Janoske U. Potential of physics-informed neural networks for solving fluid flow problems with parametric boundary conditions. Phys Fluids. 2024;36(3):037143. doi: 10.1063/5.0193952.

[34] Shi S, Liu D, Huo Z. Simulation of thermal-fluid coupling in silicon single crystal growth based on gradient normalized physics-informed neural network. Phys Fluids. 2024;36(5):053610. doi: 10.1063/5.0203775.
[35] Khan SA, Hayat T, Razaq A, Momani S. Entropy optimized flow subject to variable fluid characteristics and convective conditions. Alex Eng J. 2024;86:616–30. doi: 10.1016/j.aej.2023.11.082.
[36] Oyelakin IS, Sibanda P. A numerical study of entropy generation in radiative Casson nanofluid flow. Eng Rep. 2020;2(11):e12257. doi: 10.1002/eng2.12257.
[37] Shutaywi M, Shah Z. Mathematical modeling and numerical simulation for nanofluid flow with entropy optimization. Case Stud Therm Eng. 2021;26:101198. doi: 10.1016/j.csite.2021.101198.
[38] Rashed AS, Mahmoud TA, Mabrouk SM. Enhanced flow and temperature profiles in ternary hybrid nanofluid with gyrotactic microorganisms: A study on magnetic field, brownian motion, and thermophoresis phenomena. J Appl Comput Mech. 2024;10(3):597–609. doi: 10.22055/jacm.2024.45899.4427.
[39] Lone SA, Khan A, Gul T, Mukhtar S, Alghamdi W, Ali I. Entropy generation for stagnation point dissipative hybrid nanofluid flow on a Riga plate with the influence of nonlinear convection using neural network approach. Colloid Polym Sci. 2024;302:745–70. doi: 10.1007/s00396-024-05227-0.
[40] Prasanthi A, Shareef H, Khalid SA, Selvaraj J. Optimized forgetting factor recursive least square method for equivalent circuit model parameter extraction of battery and ultracapacitor. J Energy Storage. 2025;119:116298. doi: 10.1016/j.est.2025.116298.
[41] He X, Jia Y, Liu Y, Xia G, Li K, Lu H. Experimental investigation of film hole layout on turbine endwall along conjugate temperature gradient. Int J Therm Sci. 2025;214:109841. doi: 10.1016/j.ijthermalsci.2025.109841.
[42] Khatoon S, Phirani J, Bahga SS. Fast Bayesian inference for inverse heat conduction problem using polynomial chaos and Karhunen–Loeve expansions. Appl Therm Eng. 2023;219:119616. doi: 10.1016/j.applthermaleng.2022.119616.
[43] Pulch R. Model order reduction and low-dimensional representations for random linear dynamical systems. Math Computers Simul. 2018;144:1–20. doi: 10.1016/j.matcom.2017.05.007.
[44] Chandra A, Chevyrev I, Hairer M, Shen H. Langevin dynamic for the 2D Yang–Mills measure. Publ.math.IHES. 2022;136:1–147. doi: 10.1007/s10240-022-00132-0.
[45] Ni BY, Jiang C, Li JW, Tian WY. Interval K-L expansion of interval process model for dynamic uncertainty analysis. J Sound Vib. 2020;474:115254. doi: 10.1016/j.jsv.2020.115254.
[46] Rui EZ, Zeng GZ, Ni YQ, Chen ZW, Hao S. Time-averaged flow field reconstruction based on a multifidelity model using physics-informed neural network (PINN) and nonlinear information fusion. Int J Numer Methods Heat Fluid Flow. 2024;34(1):131–49. doi: 10.1108/HFF-05-2023-0239.
[47] Kiyani E, Kooshkbaghi M, Shukla K, Koneru RB, Li Z, Bravo L, et al. Characterization of partial wetting by CMAS droplets using multiphase many-body dissipative particle dynamics and data-driven discovery based on PINNs. J Fluid Mech. 2024;985:A7. doi: 10.1017/jfm.2024.270.
[48] Soibam J, Aslanidou I, Kyprianidis K, Fdhila RB. Inverse flow prediction using ensemble PINNs and uncertainty quantification. Int J Heat Mass Transf. 2024;226:125480. doi: 10.1016/j.ijheatmasstransfer.2024.125480.
[49] Yoo Y, Jung UJ, Han YH, Lee J. Data augmentation-based prediction of system level performance under model and parameter uncertainties: Role of designable generative adversarial networks (DGAN). Reliab Eng Syst Saf. 2021;206:107316. doi: 10.1016/j.ress.2020.107316.
[50] Son H, Cho SW, Hwang HJ. Enhanced physics-informed neural networks with Augmented Lagrangian relaxation method (AL-PINNs). Neurocomputing. 2023;548:126424. doi: 10.1016/j.neucom.2023.126424.
[51] Jang B, Kaptanoglu AA, Gaur R, Pan S, Landreman M, Dorland W. Grad–Shafranov equilibria via data-free physics informed neural networks. Phys Plasmas. 2024;31(3):032510. doi: 10.1063/5.0188634.
[52] Chandra P, Das R. Design of a unified physics-informed neural network using interior point algorithm to study the bioconvection nanofluid flow via stretching surface. Eng Appl Artif Intell. 2024;133:108647. doi: 10.1016/j.engappai.2024.108647.
[53] Jawad M, Ahmad A, Zafar H, Fu Z, Alshehery S, Junaid M, et al. Physics-informed neural networks for rotating EMHD flow of Jeffrey hybrid nanofluid with arrhenius activation energy and mass convections. Expert Syst Appl. 2025;271:126517. doi: 10.1016/j.eswa.2025.126517.
[54] Bhaumik B, Changdar S, Chakraverty S, De S. Effects of viscosity and induced magnetic fields on weakly nonlinear wave transmission in a viscoelastic tube using physics-informed neural networks. J Phys Fluids. 2024;36(12):121902. doi: 10.1063/5.0235391.
[55] Yang L, Meng X, Karniadakis GE. B-PINNs: Bayesian physics-informed neural networks for forward and inverse PDE problems with noisy data. J Comput Phys. 2021;425:109913. doi: 10.1016/j.jcp.2020.109913.
[56] Tawfik MM. Experimental studies of nanofluid thermal conductivity enhancement and applications: A review. Renew Sustain Energy Rev. 2017;75:1239–53. doi: 10.1016/j.rser.2016.11.111.
[57] Bararnia H, Esmaeilpour M. On the application of physics informed neural networks (PINN) to solve boundary layer thermal-fluid problems. Int Commun Heat Mass Transf. 2022;132:105890. doi: 10.1016/j.icheatmasstransfer.2022.105890.
[58] Groetsch CW. The theory of Tikhonov regularization for Fredholm equations. 1st edn. Boston: Pitman Advanced Pub. Program; 1984.
[59] Courant R, Hilbert D. Methods of mathematical physics: Partial differential equations. 1st edn. New York: Interscience Publishers Inc; 1953.
[60] LeCun Y, Bengio Y, Hinton G. Deep learning. Nature. 2015;521:436–44. doi: 10.1038/nature14539.
[61] Qiao H, Cheng A. A fast finite difference/RBF meshless approach for time fractional convection-diffusion equation with non-smooth solution. Eng Anal Bound Elem. 2021;125:280–9. doi: 10.1016/j.enganabound.2021.01.011.
[62] Suresh S, Venkitaraj KP, Hameed MS, Sarangan J. Turbulent heat transfer and pressure drop characteristics of dilute water based Al_2O_3-Cu hybrid nanofluids. J Nanosci Nanotechnol. 2014;14:2563–72. doi: 10.1166/jnn.2014.8467.

Appendix

A1 Two-dimensional unsteady convection–diffusion

The PINN iteration log is shown in the Figure A1.

The iterative curve of the BIPINN prediction process is shown in Figure A2.

A2 3D steady-state heat conduction with internal heat source

COSMOL verification: Heat transfer simulation was conducted using the commercial finite element software COSMOL. First, the control equations and boundary conditions were established. Second, mesh sensitivity analysis was carried out. Finally, the flow and heat dissipation performance of the channels were compared with temperature as the evaluation index. In addition, the velocity and temperature distribution cloud diagrams were combined to deeply analyze the influence of different topological channels on the convective heat performance.

A2.1 Finite element model description

The finite element model under the condition of uniform heat source is shown in Figure. The aluminum alloy liquid-cooled plate is placed on the upper surface of the copper heating plate. The copper heating plate has an embedded stainless steel heating tube, which generates heat uniformly. The heat is transferred to the liquid-cooled plate through the thermal grease layer on the contact surface. The cooling medium maintains a constant temperature at the inlet and flows under the pressure difference between the inlet and outlet of the liquid-cooled plate to carry away the heat.

A2.2 Control equations

To reduce the computational cost, the model satisfies the following assumptions: (1) The fluid is incompressible and laminar; (2) The fluid-solid boundary is a no-slip boundary; (3) The gravitational effect is ignored. The control equations are as follows:

Continuity equation:

$$\rho\nabla\cdot\mathbf{u} = 0, \tag{A1}$$

Momentum conservation equation:

$$\rho\left(\frac{\partial\mathbf{u}}{\partial t} + \mathbf{u}\cdot\nabla\mathbf{u}\right) = -\nabla p + \mu\nabla^2\mathbf{u} + \mathbf{f}, \tag{A2}$$

Energy conservation equation:
Fluid domain:

$$\rho c_p(\mathbf{u}\cdot\nabla)T = \nabla\cdot(k_f\nabla T), \tag{A3}$$

Solid domain

$$0 = \nabla\cdot(k_s\nabla T), \tag{A4}$$

where $\mathbf{u}$ represents the flow velocity, k_s represents the thermal conductivity of the solid, and k_f represents the thermal conductivity of the fluid.

A2.3 Boundary conditions

The boundary conditions of the simulation model are set as follows:

(1) The inlet flow rate is calculated based on the Reynolds number.
(2) The outlet pressure is 0.
(3) The total heating power is 200 W.
(4) The inlet liquid temperature is 20°C.
(5) The boundary between the heating plate and the liquid cooling plate is a thermal contact boundary.
(6) All other boundaries are adiabatic boundary conditions.

The heat contact control equation is shown as equation (5)

$$\begin{aligned} -\mathbf{n}_d\cdot(-k_d\nabla T_d) &= -h_{eq}(T_u - T_d) + rQ_b \\ -\mathbf{n}_u\cdot(-k_u\nabla T_u) &= -h_{eq}(T_d - T_u) + (1-r)Q_b \end{aligned}, \tag{A5}$$

where k_u and k_d are the thermal conductivity coefficients of the upper and lower contact surfaces, respectively. T_u and T_d are the temperatures of the upper and lower contact surfaces, respectively.

h_{eq} is the equivalent heat transfer coefficient, which can be expressed as follows:

$$h_{eq} = \frac{k_{eq}}{d_s}, \tag{A6}$$

where k_eq is the equivalent thermal conductivity, d_s is the thickness of the thermal contact layer. In this work, d_s = 200 μm, and Q_b represents the frictional heat. r_u and r_d are the proportionality coefficients of the upper and lower parts of the thermal contact, respectively. The calculation formula is

Table A1: Physical properties of 0.1% Cu-Al_2O_3/water HNFs and aluminum alloys

	0.1% Cu-Al_2O_3/water HNFs	Aluminum alloy
ρ [kg m^{-3}]	1001.3	$2{,}736 - 9.41 \times 10^{-3}T + 6.04 \times 10^{-4}T^2 - 8.99 \times 10^{-7}T^3 - 5.41 \times 10^{-10}T^4$
k [W m^{-1} K^{-1}]	0.62	$30.7 - 0.875T - 2.14 \times 10^{-3}T^2 + 2.05 \times 10^{-6}T^3$
C_p [J kg^{-1} K^{-1}]	4176.83	$-265 + 9.29T - 1.21 \times 10^{-}T^2 - 6.74 \times 10^{-5}T^3 + 1.65 \times 10^{-7}T^4$
μ [kg m^{-1} s^{-1}]	0.000972	—

$$r_d = \frac{1}{1+\xi_d}\xi_d = \sqrt{\frac{\rho_u C_{p,u} k_u}{\rho_d C_{p,d} k_d}} \quad r_u = \frac{1}{1+\xi_u} \quad \xi_u = \sqrt{\frac{\rho_d C_{p,d} k_d}{\rho_u C_{p,u} k_u}}, \tag{A7}$$

where $\rho_u, \rho_d, C_{p,u}, C_{p,d}, k_u, k_d$, respectively, represent the density ρ, specific heat C_p, and thermal conductivity k of the upper and lower heat contact surfaces. Material distribution variable is $\xi \epsilon [0, 1]$

The cooling working medium is 0.1% Cu-Al_2O_3/water HNFs. The material of the liquid cooling plate is aluminum alloy, the stainless steel heating tube is made of 304 steel, and the material of the heating plate is copper. The thermal physical properties of the four materials are based on (COMSOL MULTIPHYSICS 5.3A C 1.2017), as shown in Tables A1 and A2.

A2.4 Grid sensitivity analysis

This study adopts boundary layer elements to enhance the simulation accuracy at the fluid–solid interface. To avoid simulation errors caused by grid quality, a grid sensitivity analysis is necessary. When the number of elements continuously increases and eventually meets the following conditions:

$$|(p_{im}^m - p_{in}^{m+1})/p_{im}^m| \le 2.0\%, |(T_{pak}^m - T_{pak}^{m+1})/T_{pak}^m| \le 2.0\%,$$

where m represents the grid sensitivity analysis index. The grid sensitivity analysis of the straight channel liquid cooling plate is shown in Table A3. When the number of elements reaches 5,124,230, the inlet pressure p_{in} and the peak temperature T_{peak} tend to remain unchanged. Therefore, there is no need to further refine the grid (for, details, refer Table A3).

A.2.5 Analysis of numerical simulation results under single heat source conditions

Based on the velocity field distribution, pressure field distribution, and temperature field distribution of the liquid-cooled channel cross-sections obtained after topology optimization by COSMOL, we can analyze the impact of different channel designs on heat transfer efficiency. These distributions provide insights into how the flow dynamics and thermal characteristics vary across the channel, which is crucial for optimizing the design of heat exchangers and enhancing their performance.

A3 3D unsteady heat conduction

A.3.1 Velocity boundary

The velocity field needs to satisfy the hydrodynamic boundary conditions as follows:

No-slip condition: The velocity of the fluid on the solid wall is zero, as shown below:

$$\mathbf{u}(x, y, z, t)|_{\text{wall}} = 0. \tag{A8}$$

Table A2: Physical properties of stainless steel 304 and copper

	Stainless Steel 304	Copper
ρ [kg m^{-3}]	8,030	8,960
k [W m^{-1} K^{-1}]	$11.702649 + 0.012955T$	400
C_p [J kg^{-1} K^{-1}]	$114.227517 + 1.877902T - 0.003234T^2 + 3.0 \times 10^{-6}T^3 - 8.0 \times 10^{-10}T^4$	385
μ [kg m^{-1} s^{-1}]	—	—

Table A3: Grid sensitivity analysis of liquid cooling plate example (Re = 150, Q = 200 W)

Number of units	p_{in} (Pa)	$\lvert(p_{in}^{m} - p_{in}^{m+1})/p_{in}^{m}\rvert$	$T_{surf,max}$ (°C)	$\lvert(T_{susf,max}^{m} - T_{susf,max}^{m+1})/T_{susf,max}^{n}\rvert$	Time (min)
35,294	2.3776	—	82.427	—	<1
114,795	2.2562	5.11%	78.828	4.36%	1
281,278	2.2728	0.74%	76.662	2.75%	4
596,021	2.2385	1.51%	75.111	2.02%	6
2,013,586	2.2015	1.65%	73.615	1.99%	10
5,124,230	2.1745	1.23%	72.434	1.60%	30

Free-stream condition: Away from the wall, the fluid velocity reaches the free-flow velocity, as shown below:

$$\mathbf{u}(x, y, z, t)|_{\text{free-stream}} = \mathbf{U}_{\infty}. \tag{A9}$$

Loss function:

$$\mathcal{L}_{\text{velocity}} = \sum_{i\in\text{wall}} \mathbf{u}(x_i, y_i, z_i, t_i) - 0_2^2 + \sum_{j\in\text{free-stream}} \mathbf{u}(x_j, y_j, z_j, t_j) - \mathbf{U}_{\infty 2}^2. \tag{A10}$$

A3.2 Experimental verification

To further explore and verify the thermal properties of 3D unsteady-state heat conduction, we set up a liquid cooling circulation experimental system and compared it with the temperature field distribution predicted by BIPINN.

A.3.2.1 Experimental system architecture and equipment selection

The purpose of building the liquid cooling circulation experimental system is to record the fluid flow state inside the liquid cooling channel and the heat dissipation characteristics of the liquid cooling plate when the fluid-solid conjugate heat transfer reaches a stable state. To achieve this goal, the experimental system mainly consists of a liquid cooling drive source, sensors, a data acquisition device, an infrared thermal imager, and a heating system. Figure A1 shows the schematic diagram of the liquid cooling circulation experiment.

A.3.2.1.1 Liquid-cooled drive source

This study selects an industrial water chiller as the drive source, which directly outputs cooling working fluid at a constant temperature (0.1% Cu-Al_2O_3/water HNFs).

A.3.2.1.2 Sensors and data acquisition devices

Sensors and data acquisition devices are used to detect and record the fluid flow characteristics and the heat dissipation performance of the liquid-cooled plate. The fluid flow characteristics include the flow rate in the pipeline; the heat dissipation characteristics include the temperature distribution of the liquid-cooled plate, and the fluid temperature at the inlet and outlet of the liquid-cooled plate.

This study focuses on steady laminar flow (Reynolds number Re < 2,300), with Re set at 150 and the length of the liquid-cooled plate being 0.1 m. According to the definition of the Reynolds number, it can be calculated that

$$\text{Re} = \frac{\rho U L}{\mu}. \tag{A11}$$

The velocity can be solved using equation (11) as follows:

$$U = \frac{\text{Re}\cdot\mu}{\rho\cdot L} = \frac{150\times 0.972\times 10^{-3}}{1001.3\times 0.1} \approx 0.0014\frac{\text{m}}{\text{s}}. \tag{A12}$$

The inlet cross-sectional area is 0.001m^2.

The inlet flow rate is the product of the velocity and the inlet cross-sectional area $1.4\times10^{-6}\text{m}^3/s$.

Based on this, the flow rate in the pipeline does not exceed 1.5 L/min. Therefore, in this study, the Omegaflv-4605A mass flowmeter (with a range of 0.04–2 L/min and an accuracy of 0.2%) is selected to measure the flow rate in the pipeline. The water temperatures at the inlet and outlet ends of the liquid cooling plate are monitored by PT100 temperature sensors. The data collector is FLUKE Tiss55+. The 0–20 mA signals output by the sensors are transmitted to the paperless recorder and then converted into analog signals for data storage.

A.3.2.1.3 Infrared thermal imager

Commonly used temperature measurement devices include thermocouples and infrared thermal imagers.

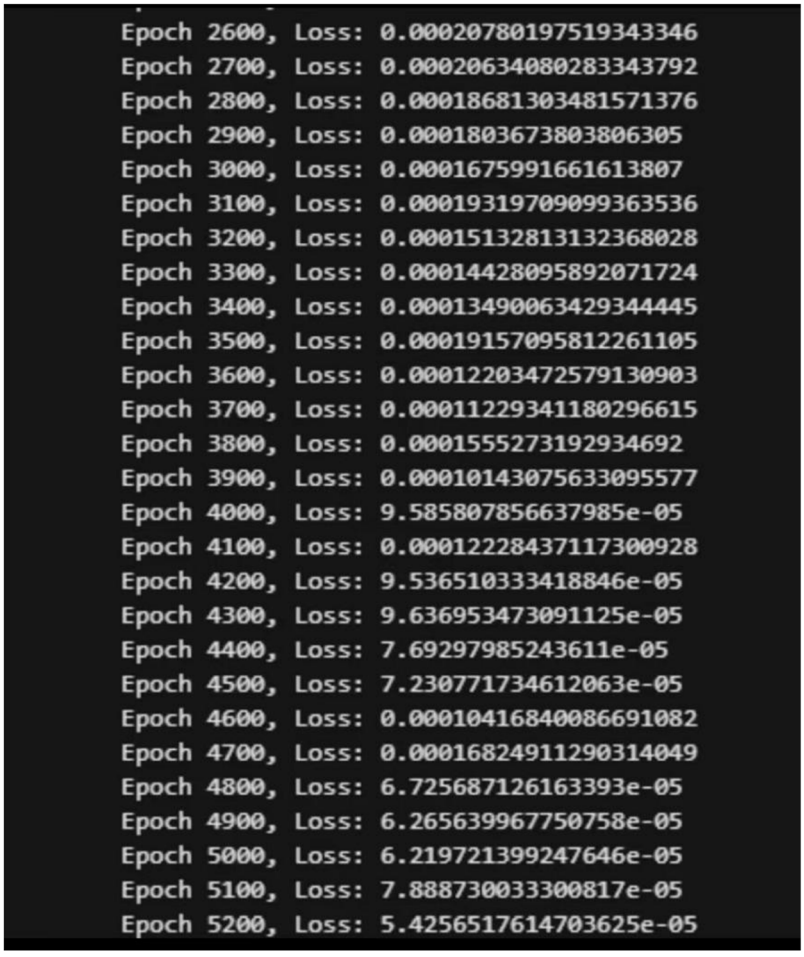

Figure A1: The number of iterations of PINN until reaching the 10^{-5} level.

This study adopts the infrared thermal imager FLUKE Tis55+ to measure the temperature of the object from a certain distance to evaluate the heat dissipation characteristics of the liquid cold plate. It can capture the temperature field distribution cloud map on the surface of the object. This study focuses on comparing the influence

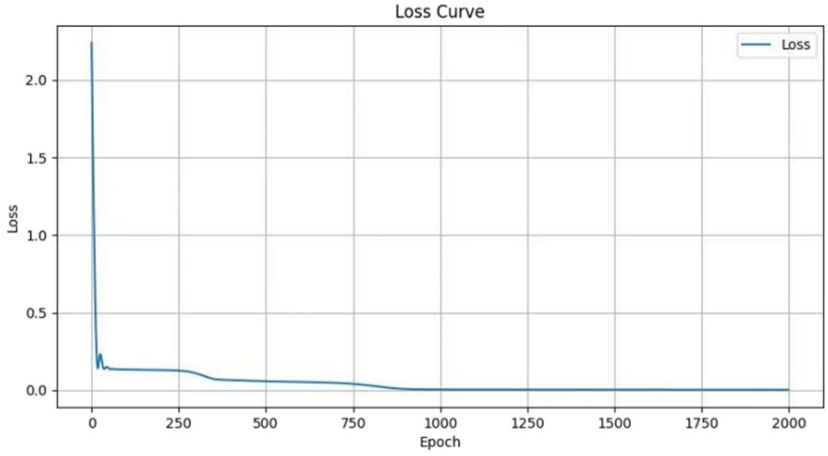

Figure A2: The loss curve of BIPIN.

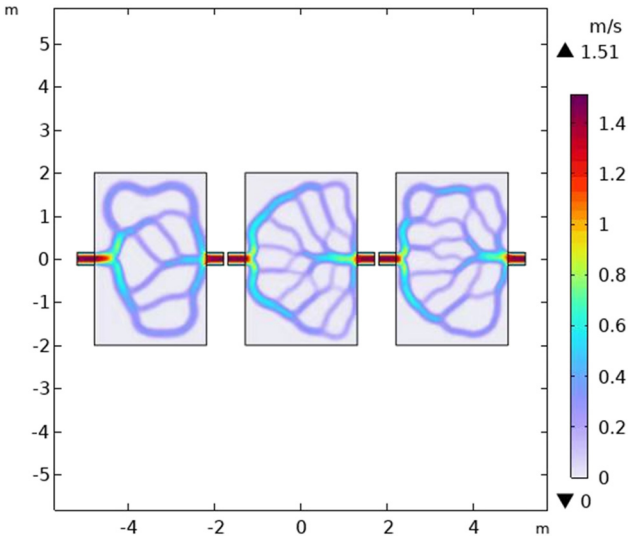

Figure A3: Cloud diagrams of velocity field distribution of liquid cooling channel cross-sections after different topology optimizations.

of mixed NFs on the heat dissipation characteristics of the liquid cold plate. The temperature field distribution on the surface of the liquid cold plate is more intuitive, and the absolute value of the temperature within a certain error range is acceptable.

A.3.2.1.4 Heating system

The heater is placed at the bottom of the liquid-cooled plate, providing a constant heat generation rate. Its working principle is the electrothermal effect: when current passes through a conductor, heat is generated and transferred out by the conductor. In this study, the heating rods are connected in parallel between the power supply terminals. The product of the current and voltage is the heating power, and the heat generation rate is controlled by a voltage regulator.

A3.3.1 Experimental scheme

The heat generation rate is kept constant at Q = 200 W by a voltage regulator. The flow rate in the pipeline is adjusted through a valve. The temperature field distribution on the surface of the liquid cooling plate is recorded respectively when the flow rate is from 1.2 L/min to 0.2 L/min. To ensure that the fluid heat transfer reaches a steady state during the experiment, the data recording should be conducted when the maximum temperature fluctuation captured by the infrared thermal imager on the upper surface of the liquid cooling plate does not exceed ±0.15°C.

A3.3.2 Experimental procedures

1) Turn on the industrial water chiller, adjust the liquid temperature to 20°C, and expel the air bubbles in the pipeline.
2) Slowly adjust the valve to stabilize the inlet flow rate at 1 L/min.
3) Turn on the heating device, slowly adjust the pressure regulator, record the current and voltage values, and keep the heat flux constant at 200 W.
4) Determine whether the system has reached a stable state through the flowmeter and infrared thermal imager.
5) After reaching a steady state, use the thermal infrared imaging camera to capture the temperature cloud map on the upper surface of the liquid-cooled plate.
6) Slowly adjust the valve to reduce the flow rate in the pipeline, repeat steps (4)–(6), and re-record the data.
7) Turn off the heating system, maintain the liquid cooling circulation for a period of time until the cold plate and heating plate return to room temperature, turn off the water chiller, and clean the residual liquid in the test system.

A4 BIPINN under multi-physics field effects

A feedforward neural network is constructed, with the input being spatial and temporal coordinates (ə, t), ə ∈ (x, y, z), and the output being the fluid flow field F(ə, t) temperature field T(ə, t) and concentration field C(ə, t). The hidden layer is 8 layers with 20 nodes per layer, and the activation function is usually chosen to be the hyperbolic tangent function (Tanh).

Components of the loss function in this study: The loss function consists of three parts, namely, the initial condition loss, PDE residual loss, and boundary condition loss. This multi-part loss function design enables the model to not only fit the data but also satisfy physical laws and boundary conditions.

The PDE residuals are calculated using automatic differentiation techniques and reflect the deviation between the network's predictions and the physical laws.

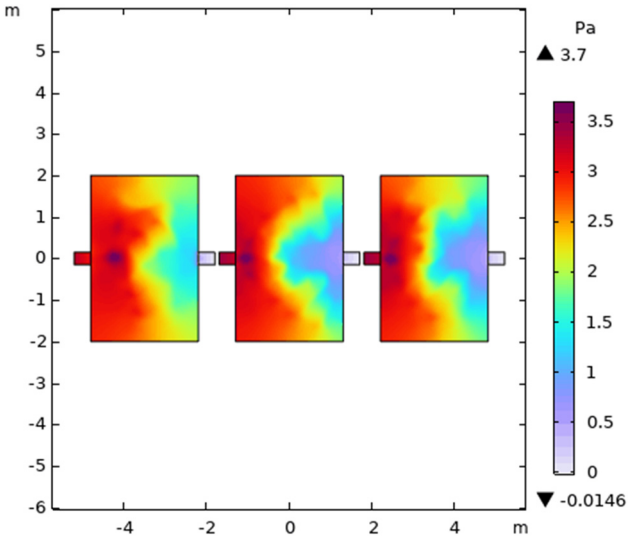

Figure A4: Cloud diagrams of pressure field distribution in cross-sections of liquid cooling channels after different topology optimizations.

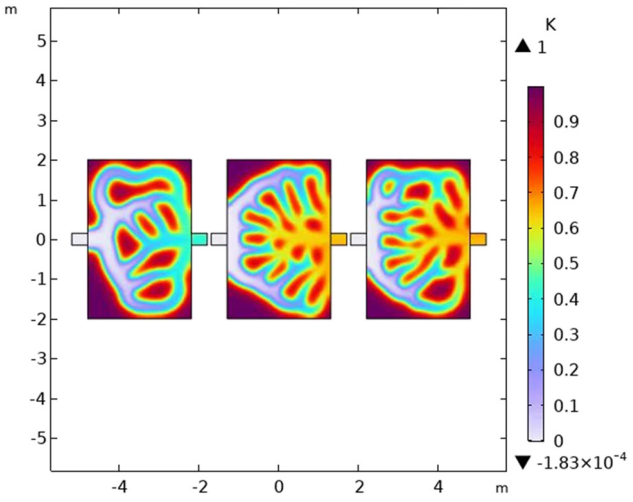

Figure A5: Cloud diagrams of temperature field distribution of liquid cooling channel cross-sections after different topology optimizations.

The expression for the loss function is

$$L = w_1 L_{\mathrm{PDE}} + w_2 L_{\mathrm{BC}} + w_3 L_{\mathrm{IC}}, \tag{A13}$$

where L_{PDE}, L_{BC}, and L_{IC} respectively represent the MSEs of the PDE residual, boundary conditions, and initial conditions. w_1, w_2, and w_3, are weights used to balance the losses of each part.

Momentum conservation equation:

$$\rho\left(\frac{\partial \mathbf{u}}{\partial t} + \mathbf{u}\cdot\nabla\mathbf{u}\right) = -\nabla p + \mu\nabla^2\mathbf{u} + \mathbf{f}, \tag{A14}$$

where ρ represents the fluid density, $\mathbf{u}$ is the velocity vector, p is the pressure, μ is the dynamic viscosity coefficient, and $\mathbf{f}$ is the volume force (such as gravity, electromagnetic force, *etc.*).

Energy conservation equation:

$$\rho c_{\mathrm{p}}\left(\frac{\partial T}{\partial t} + \mathbf{u}\cdot\nabla T\right) = k\nabla^2 T + Q, \tag{A15}$$

where c_{p} is the specific heat capacity, T is the temperature, k is the thermal conductivity, and Q represents the internal heat source (such as heat release from chemical reactions, *etc.*).

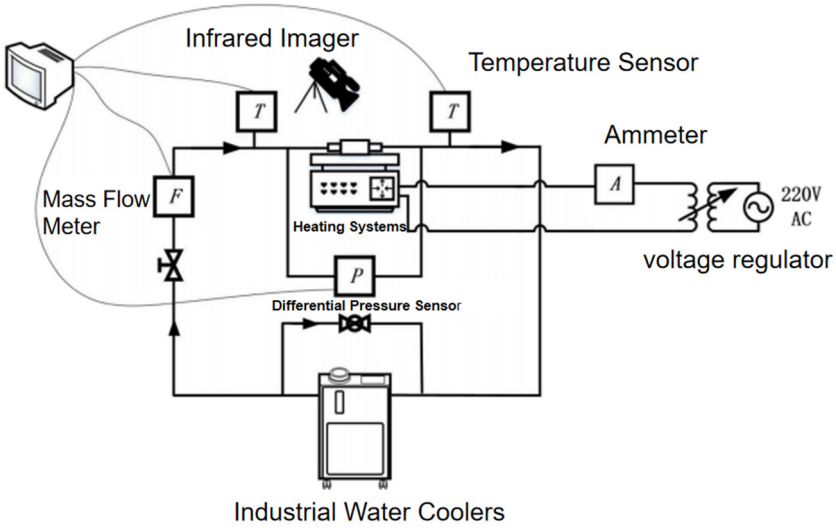

Figure A6: Schematic diagram of the liquid cooling circulation experiment.

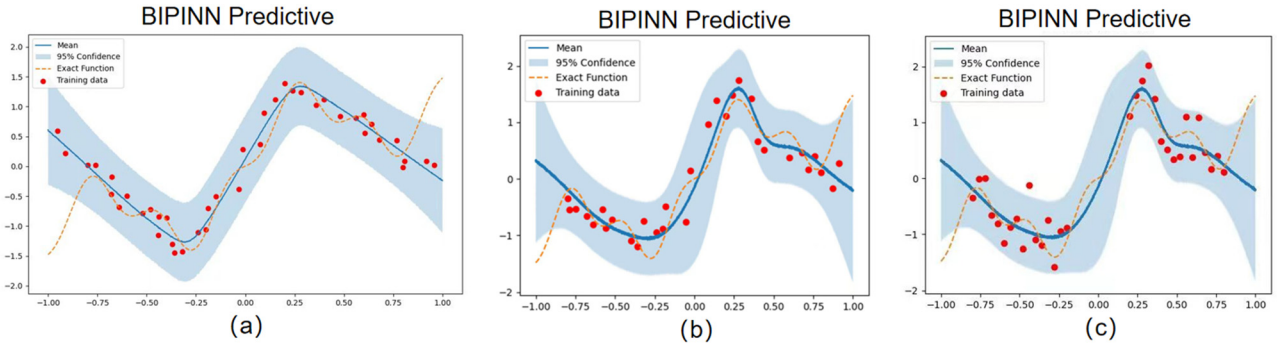

Figure A7: (a–c) The multi-physics prediction results of BIPINN.

The concentration distribution of nanoparticles can be described by a similar diffusion–convection equation:

$$\frac{\partial C}{\partial t} + \mathbf{u} \cdot \nabla C = \nabla \cdot (D \nabla C), \tag{A16}$$

where C represents the concentration of nanoparticles and D is the diffusion coefficient.

Loss function setting:

Residuals from the physics equations: This part of the loss ensures that the output of the neural network satisfies the control equations. For the nanofluid flow problem, the residuals of the physical equations can be expressed as:

$$\xi_{\text{PDE}} = \frac{1}{N_{\text{r}}} \sum_{i=1}^{N_{\text{r}}} (\text{Nu}_{\text{NN}}(x_i) - R(x_i))^2, \tag{A17}$$

where $\text{Nu}_{\text{NN}}(x_i)$ is the approximate solution of the physical equation by the neural network, $R(x_i)$ is the known form of the physical equation, and N_{r} is the number of sampling points.

Residual of boundary conditions: This part of the loss ensures that the output of the neural network satisfies the boundary conditions. The residuals of the boundary conditions can be expressed as

$$\xi_{\text{BC}} = \frac{1}{N_{\text{b}}} \sum_{i=1}^{N_{\text{b}}} (u_{\text{NN}}(x_i) - Q(x_i))^2, \tag{A18}$$

where $u_{\text{NN}}(x_i)$ is the output of the neural network, $Q(x_i)$ is the known value of the boundary condition, and N_{b} is the number of boundary sampling points.

For no-slip boundary conditions,

$$\mathcal{L}_{\text{bc}} = \|\mathbf{u}(x = 0, y, z, t) - 0_2^2\| + \|\mathbf{u}(x = L, y, z, t) - U_2^2\|, \tag{A19}$$

where L is the pipe length and U is the inlet velocity.

For temperature boundary conditions,

$$\mathcal{L}_{\text{bc}} = \|T(x = 0, y, z, t) - T_0\|_2^2 + \|T(x = L, y, z, t) - T_L\|_2^2. \tag{A20}$$

To assess how well the neural network's outputs align with the physical equations, we evaluate certain criteria. This evaluation helps us understand if the network predictions accurately reflect the expected behavior as dictated by the physical laws governing fluid dynamics, energy conservation, and nanoparticle transport.

For the flow equation,

$$\mathcal{L}_{\text{NS}} = \left\| \rho \left(\frac{\partial \mathbf{u}}{\partial t} + \mathbf{u} \cdot \nabla \mathbf{u} \right) + \nabla p - \mu \nabla^2 \mathbf{u} - \mathbf{f}_2^2 \right\|. \tag{A21}$$

For the energy equation,

$$\mathcal{L}_{\text{energy}} = \left\| \rho c_p \left(\frac{\partial T}{\partial t} + \mathbf{u} \cdot \nabla T \right) - k \nabla^2 T - Q_2^2 \right\|. \tag{A22}$$

For the nanoparticle transport equation,

$$\mathcal{L}_{\text{particle}} = \left\| \frac{\partial \phi}{\partial t} + \mathbf{u} \cdot \nabla \phi - D_b \nabla^2 \phi_2^2 \right\|, \tag{A23}$$

Based on the above conditions, the predicted physical field of the hot channel of BIPINN after topology optimization is obtained, as shown in Figure A7.

The prediction of physical fields, which includes multiple factors such as flow velocity, temperature, and pressure, and the interactions among them, we also comprehensively considered various factors when setting the loss function, thus obtaining the prediction results of multi-physical fields.